

Characterizing the seasonal cycle of upper-ocean flows under multi-year sea ice



Jean A. Mensa*, M.-L. Timmermans

Department of Geology and Geophysics, Yale University, 210 Whitney Ave, New Haven CT 06511, USA

ARTICLE INFO

Article history:

Received 18 September 2016

Revised 7 March 2017

Accepted 18 March 2017

Available online 29 March 2017

Keywords:

Mixed layer
Arctic ocean
Submesoscale
Sea ice

ABSTRACT

Observations in the Arctic Ocean suggest that upper-ocean dynamics under sea ice might be significantly weaker than in the temperate oceans. In particular, observational evidence suggests that currents developing under sea ice present weak or absent submesoscale ($\mathcal{O}(1)$ Rossby number) dynamics, in contrast with midlatitude oceans typically characterized by more energetic dynamics at these scales. Idealized numerical model results of the upper ocean under multi-year sea ice, subject to realistic forcing, are employed to describe the evolution of the submesoscale flow field. During both summer and winter under multi-year sea ice, the simulated submesoscale flow field is typically much less energetic than in the midlatitude ice-free oceans. Rossby numbers under sea ice are generally consistent with geostrophic dynamics ($Ro \sim \mathcal{O}(10^{-3})$). During summer, ice melt generates a shallow mixed layer ($\mathcal{O}(1)$ m) which isolates the surface from deeper, warmer and saltier waters. The Ekman balance generally dominates the mixed layer, although inertial waves are present in the simulations during weakening and reversals of the ice-ocean stress. During winter, mixed-layer deepening (to about 40 m depth), is associated with convection driven by sea-ice growth, as well as ice-ocean shear-driven entrainment at the base of the mixed layer. Submesoscale activity is observed to develop only rarely, when winter convective mixing is laterally inhomogeneous (i.e., in the presence of sea-ice leads or spatially inhomogeneous sea-ice thickness) and when this coincides with weak ice-ocean shear-driven mixing. These submesoscale features are diagnosed with particular focus on their implications for ocean-to-ice heat fluxes.

© 2017 Elsevier Ltd. All rights reserved.

1. Introduction

Submesoscale (SM) flows, characterized by Rossby number $\mathcal{O}(1)$ and horizontal scales between 100 m and 10 km in the mid-latitudes, have been shown to play an important role in the upper-ocean dynamics of most major ocean basins. Submesoscale features are known to develop in weak stratification regimes, such as the ocean mixed layer, and in the presence of a source of available potential energy such as: at major ocean fronts (e.g., Gula et al., 2014; Veneziani et al., 2014), along density gradients generated by river outflows (e.g., Luo et al., 2016), around mesoscale eddies (e.g., Mensa et al., 2013; Sasaki et al., 2014), and in regions of coastal upwelling (e.g., Capet et al., 2008d).

Baroclinic instabilities developing in the presence of weak stratification and a reservoir of available potential energy can generate features with large Rossby numbers and strong vertical velocities (Stone, 1966; Boccaletti et al., 2007). Due to their ageostrophic nature, SM features are thought to play an important role in the

ocean energy budget, providing a pathway for forward energy dissipation (Muller et al., 2005; McWilliams, 2008; Molemaker et al., 2010). Given the large vertical velocities that SM flows can generate, SM features are also thought to be responsible for a significant fraction of the observed primary production in the oceans (Lévy et al., 2001; Mahadevan and Tandon, 2006; Mahadevan et al., 2008; McGillicuddy et al., 2007; Klein and Lapeyre, 2009), driving for vertical transport of nutrients into the euphotic zone. SM features are also of significance to lateral material transport in the ocean (e.g., Lumpkin and Elipot, 2010; Poje et al., 2014). Lateral transport by SM flows has important practical consequences to the fate of pollutants (e.g., oil spills) pointing to the need for numerical simulations and observations to resolve these small scale flows (Mensa et al., 2015).

While there has been much progress in developing an understanding of SM dynamics in the midlatitude ice-free oceans, little is known about this flow regime in the Arctic Ocean. SM features may impact on sea ice, primary production, lateral transport of nutrients and pollutants, and the upper-ocean heat budget. Sea-ice cover is influenced by heat fluxes at the base of the ocean mixed layer where a reservoir of ocean heat exists underlying a rela-

* Corresponding author.

E-mail addresses: jmensa@yale.edu, jean.mensa@yale.edu (J.A. Mensa).

tively cool fresh mixed layer (e.g., Maykut, 1982; Wettlaufer, 1991; McPhee, 1992; Perovich and Elder, 2002). Small-scale flows associated with vertical velocities that might enhance ocean-to-ice heat fluxes could have serious consequences to sea-ice cover. Similarly, lateral transport of ocean heat by SM flows could enhance sea-ice melt, a process largely underestimated by general circulation models (Serreze, 2007; Stroeve et al., 2007; Rampal et al., 2011) and of crucial importance in the understanding of present and future global climate (e.g., Walsh, 1983; Budikova, 2009). Further, in an Arctic undergoing rapid change, and expansion of activities such as oil exploration, understanding pollutant dispersal in the upper ocean is of utmost importance (National Academies Report (NAS), 2014).

Observations in the Arctic Ocean suggest that the energetics of upper-ocean flows under sea ice, and in ice-free regions of the Chukchi Sea, might be different from those of the temperate oceans (Timmermans and Winsor, 2013; Timmermans et al., 2012). In contrast with midlatitude oceans characterized by energetic upper ocean dynamics at submesoscales (Capet et al., 2008b; Mensa et al., 2013; Callies et al., 2015), observations suggests that submesoscale dynamics are weak under sea ice, however the generality of this statement remains unknown. For example, Timmermans et al. (2012) show that although some frontal activity is present under sea ice, horizontal wavenumber (k) spectra of potential density variance in the mixed layer exhibit steep slopes – scaling as k^{-3} for wavelengths between around 5 and 50 km, compared to the k^{-2} scaling more typical of the midlatitudes.

The presence of sea ice affects both the dynamics and thermodynamics of the upper ocean and possibly impacts the development of SM instabilities. Ice cover effectively limits the propagation of surface gravity waves and mediates wind-forced internal waves (e.g., Levine et al., 1985; Dosser et al., 2014). On the other hand, sea-ice drift can generate significant upper-ocean stresses, and enhance turbulent mixing near the surface (e.g., Denbo and Skillingstad, 1996; Backhaus and Kampf, 1999; Skillingstad, 2001; Cole et al., 2013). Buoyancy fluxes are also mediated by sea ice, with sea-ice melt and freshwater input generating a stabilizing buoyancy flux during summer, and sea-ice growth and brine rejection generating a destabilizing buoyancy flux during winter.

In this paper, we present results from an idealized high-resolution numerical simulation of the upper Arctic Ocean with the intention of exploring the seasonal cycle of the upper ocean under multi-year sea ice. Results are limited to regions of the Arctic Ocean that are permanently ice covered (i.e., areal concentration of sea ice is never below about 75%). A transition from fully ice covered to ice-free, and the intermediate marginal ice zone dynamics, are outside the scope of this study and likely present significantly different results. Here we retain the simplest possible framework avoiding the uncertainties associated with additional sea-ice parameterizations (e.g., Smedsrud and Martin, 2015). Our simulation is forced with realistic atmospheric forcing and the model produces seasonal cycles of sea ice and upper-ocean properties that are consistent with observations (Section 3). In Section 4, we show how the development of small-scale flows under sea ice does not present the typical submesoscale *soup* (Gula et al., 2014) characteristic of the midlatitudes. Instead, small-scale flows in the mixed layer under sea ice are dominated by Ekman dynamics and convective processes with little interaction between the surface mixed layer and underlying interior ocean. Two examples that demonstrate occasional development of SM features are also presented in this section; the corresponding background settings for these provides context and motivation for future study. Also in Section 4, we test the applicability of a submesoscale parameterization in the under-ice setting modeled here. In Section 5, we summarize and discuss our results, comparing and contrasting the well-known midlatitude SM regime with ocean dynamics under sea ice.

2. Numerical model configuration

Our study employs the MIT general circulation model (MITgcm, Marshall et al., 1997; Adcroft et al., 2014) in an idealized configuration. The square domain spans 256 km by 256 km in the horizontal and has a fixed depth of 700 m. Boundary conditions are doubly-periodic at the sides, with free-surface and free-slip at the surface and bottom boundaries, respectively. The model has a horizontal resolution of 500 m and vertical resolution varying from 0.2 m near the surface (over the mixed layer, mean vertical resolution ranges between 0.5 m in summer and 1.6 m in winter) to 50 m near the bottom, for a total of 52 layers. Computations were performed on the Center for Computational Sciences clusters at the University of Miami.

The model consists of an ocean component and a sea-ice component, with communication between the modules at the ice-ocean interface. The ocean component is configured to solve the hydrostatic, Boussinesq equations. We use an f -plane approximation as the β -effect is negligible near the poles. Horizontal tracer diffusivities are implicit while horizontal viscosity in the momentum equations is biharmonic and uses a Leith eddy viscosity coefficient (Leith, 1996; 1968). Vertical eddy viscosity and diffusivities are set by the non-local K-profile parameterization (KPP, Large et al., 1994). KPP enhances vertical viscosity and diffusivities when shear instabilities and convection generate mixing in the boundary layer (i.e., the mixed layer). The mixed-layer or boundary-layer depth (BLD) is set as the depth at which the bulk Richardson number equals a critical value of 0.3. A nonlinear sea-water equation of state is used to compute density (see Jackett and McDougall, 1995), which in the cold polar oceans is primarily a function of salinity (e.g., see the discussion in Timmermans and Jayne, 2016).

The ice model consists of both a dynamic and thermodynamic component, generating sea-ice stress acting on the ocean surface and buoyancy fluxes associated with its growth and melt. The sea-ice dynamics implements the model of Zhang and Hibler (1997), where internal stresses are described via a viscous plastic model (Zhang and Hibler, 1997). Ice dynamics mediates the transfer of atmospheric stresses to the ocean. Ice thermodynamics follows the model by Hibler III (1980). The model uses a zero-layer formulation, in which heat conductivity across the ice is parameterized assuming a linear ice temperature profile together with a constant ice conductivity (Semtner, 1976). Although this formulation has the tendency to underestimate the amplitude of the seasonal cycle in sea-ice thickness and extent (Semtner, 1984), we find a sea-ice seasonal cycle in good agreement with the observations described by Timmermans (2015) for the same region and time. The thermodynamics model computes sea-ice thickness (H_I) and fractional area of sea ice (A_I , defined as the area of each grid cell covered by sea-ice), and the fluxes at the ice-ocean interface.

2.1. Initial conditions and model spin-up

We initialize the ocean module with temperature and salinity typical of a weak surface front under sea ice in August in the Arctic Ocean's Canada Basin (see Timmermans et al., 2012). The initial surface front (configured as a filament, Fig. 1a) is characterized by a surface (i.e., mixed layer) horizontal density gradient of $5 \times 10^{-7} \text{ kg m}^{-4}$. The filament consists of fresher (and less dense) surface waters, while surface waters either side are saltier (and more dense). The entire surface is at the freezing temperature, which means that the filament waters are slightly warmer than the waters either side.

The front is allowed to relax (unforced and without sea ice) for 100 days in a 1 km horizontal resolution simulation; the resulting state exhibits a fully developed eddy field and is integrated

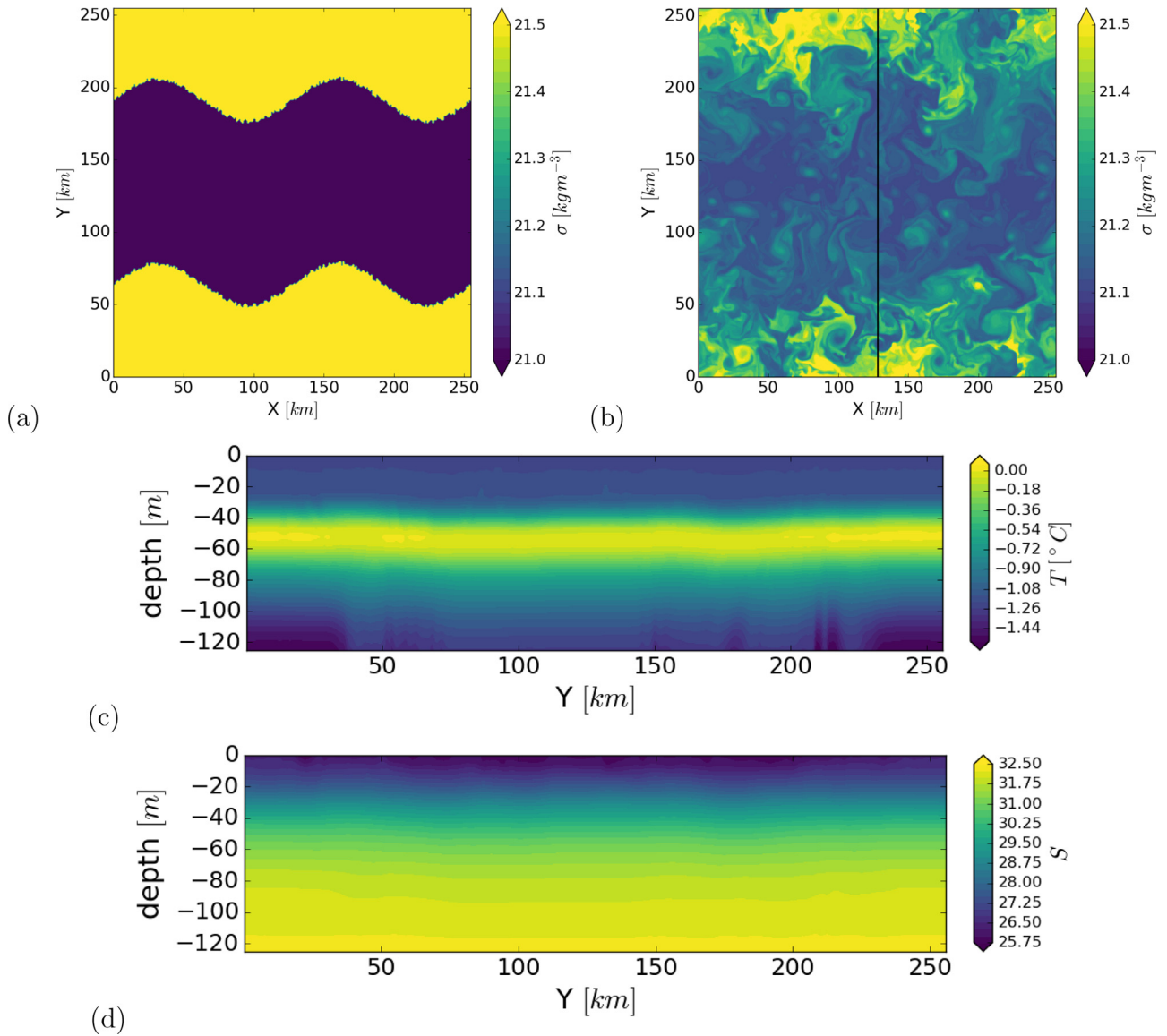


Fig. 1. Plan view of surface density anomalies [kg m^{-3}] at (a) day 0, and (b) day 110 (the initial condition for the forced simulation). Distance-depth sections of (c) temperature [$^{\circ}\text{C}$] and (d) salinity along $X = 125$ km (black line in panel b) at day 110.

again for 10 days at 500 m resolution. The final state, corresponding to the 100+10 days spin-up (Fig. 1b), is used to initialize a 2-year forced simulation under uniform sea-ice cover of 2.8 m thickness (with this initial thickness taken to be consistent with observations, (Timmermans, 2015)). To verify that the initial conditions specified here can lead to an active SM flow field, we ran the model for an extra 30 days (unforced) at 500 m resolution (after the 100 day spin up). Results in those 30 days indicate clear evidence for SM features characterized by $\mathcal{O}(1)$ Rossby numbers (i.e., the model setting permits SM).

The basic vertical stratification is a relatively cool, fresh mixed layer in the upper 40 m (Fig. 1c and d). The mixed layer is separated from a layer of warm water (between about 50 and 80 m depth) by a strong halocline at its base. The warm layer is the upper halocline of the Canada Basin, which has Pacific Ocean origins (see e.g., Toole et al., 2010; Timmermans et al., 2012; 2014, for details).

2.2. Atmospheric forcing

The model forcing is for a full year (the year 2007) using the 3-hourly European Centre for Medium-Range Weather Forecasts (ECMWF) ERA-Interim reanalysis fluxes in the region (Dee et al., 2011) with a resolution of a quarter degree; parameters are: short- and long-wave radiation, 10 m air temperature, relative humidity, net precipitation, evaporation and wind velocity. Forcing is taken over a 256 km by 256 km area with 135 $^{\circ}$ W and 80 $^{\circ}$ N taken as the upper east corner, and spatially averaged over the domain in order to avoid discontinuities at the doubly periodic boundaries.

All variables, with the exception of wind speed, show a clear seasonal cycle (as shown in Timmermans (2015)). The year 2007 is chosen in order to allow a direct comparison with the observations presented by Timmermans (2015), although the overall seasonal cycle of atmospheric forcing is similar to other years. Atmospheric forcing is applied to the 110-day state (Fig. 1b), and the model is integrated for two years, with the same annual cycle of forcing used for both the first and the second years of integration.

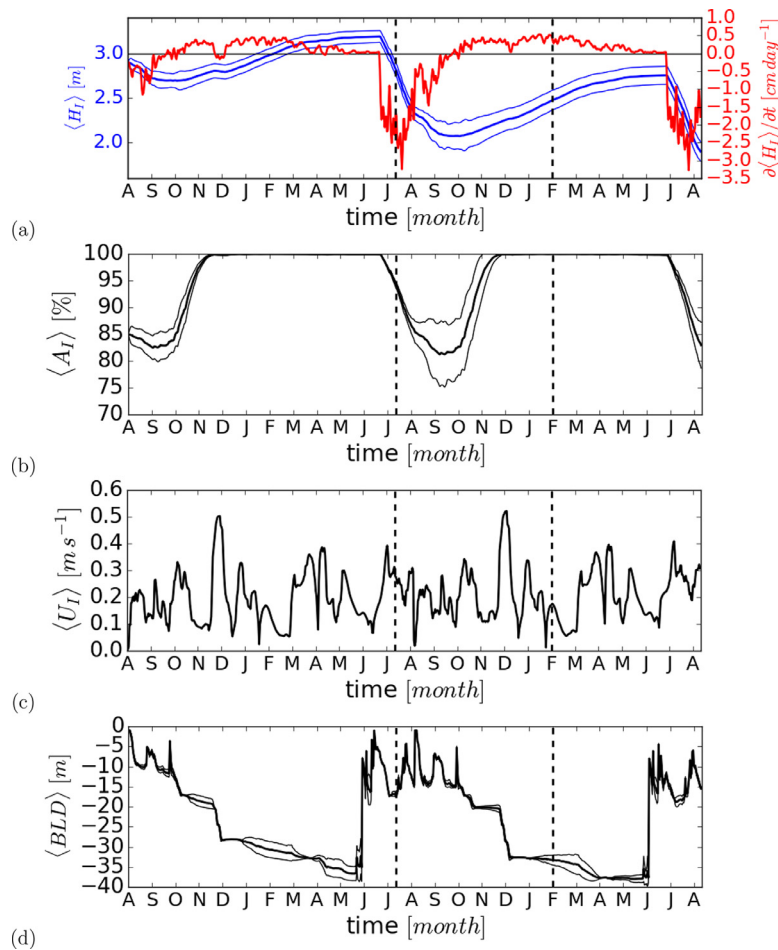


Fig. 2. Horizontally averaged (a) sea-ice thickness $\langle H_I \rangle$ [m] and melt rate $\partial \langle H_I \rangle / \partial t$ [cm day⁻¹], (b) fractional sea-ice area $\langle A_I \rangle$, (c) sea-ice drift speed $\langle U_I \rangle$ [m s⁻¹] and (d) boundary layer depth $\langle BLD \rangle$ [m] for the two years of integration. Vertical dashed lines identify representative summer (left) and winter (right) days. Thin lines in (a), (b) and (d) represent the mean ± 1 standard deviation.

3. Seasonal evolution of sea ice and the upper ocean

3.1. Sea ice

Horizontally averaged sea-ice thickness $\langle H_I \rangle$ follows a typical seasonal cycle, reaching a maximum for the year around May, and beginning to melt at a rate of about 2 cm day⁻¹ around June (Fig. 2a). Minimum thickness is attained around September/October, after which point fall/winter ice growth commences, with maximum growth rate around February. Qualitatively the seasonal cycle of $\langle H_I \rangle$ is consistent with observations from the same region (Timmermans, 2015). Horizontally averaged sea-ice fractional area $\langle A_I \rangle$ presents a corresponding seasonal cycle, decreasing shortly after the onset of melt in late June, reaching a minimum in September, and returning to 100% coverage by around December (Fig. 2b). Recall, the simulation is intended to represent conditions under the permanent sea-ice cover, and $\langle A_I \rangle$ is never smaller than about 75% whereas typical marginal-ice zone conditions might have ice cover in the range 15–70%. Horizontally averaged sea-ice drift speed $\langle U_I \rangle$ exhibits no clear seasonal cycle, with $\langle U_I \rangle$ around 0.2 m s⁻¹ (Fig. 2c). Qualitatively, $\langle U_I \rangle$ is similar to observations from the same region (Cole et al., 2013).

3.2. Upper-ocean properties

Seasonality of atmospheric forcing and sea-ice is reflected in the seasonal cycle of BLD and mixed-layer temperature T and salin-

ity S (Figs. 2d and 3; c.f., Toole et al. (2010)). Summer sea-ice melt releases fresh water at the ice-ocean interface forming a shallow summer halocline associated with a minimum BLD of about 3 m (characterized by minimum mixed-layer salinities for the year). A remnant winter mixed layer (see e.g., Jackson et al., 2010) remains below the summer mixed layer, and above the main halocline, throughout the summer and fall (Fig. 3). Winter sea-ice growth expels dense salty water (i.e., injection of brine) which deepens and salinifies the mixed layer over the course of the winter; shear-driven deepening also plays a role, as will be discussed in the next section. BLD attains a maximum of about 35 m in the winter months, consistent with winter observations in the Canada Basin (e.g., Toole et al., 2010; Timmermans, 2015). The mixed layer is bounded during winter by the main halocline and underlying warm water with occasional entrainment events of this warm water into the mixed layer (Fig. 3). These sub-ice mixed layers are generally shallower with a smaller seasonal range than those in ice-free oceans; for example, Kara (2003) reports global BLDs between 65°N and 72°S showing a range between a few meters in summer to several hundred meters in winter.

The temperature of the mixed layer remains close to the freezing temperature (T_f , a linear function of salinity) throughout the simulation, with deviations to warmer temperatures in the summer months after the onset of seasonal melt when A_I decreases from 100% and penetrating short-wave radiation warms the surface ocean (Fig. 3b). Other instances of temperature in excess of freezing occur sporadically in the winter months (Fig. 3b), and appear

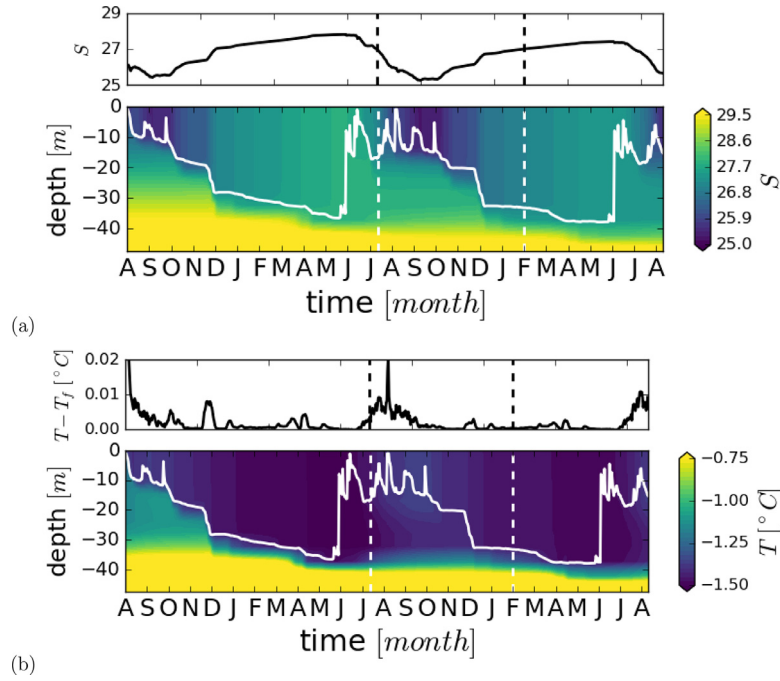


Fig. 3. Horizontally averaged time-depth sections of (a) salinity and (b) temperature [°C] over the two-year integration. The solid white line represents the BLD and the dashed white lines the representative summer and winter days. Time series of horizontally-averaged salinity S and $T - T_f$ (mixed-layer temperature above the freezing temperature T_f) at 2 m depth are shown above each section.

to be associated with shear-driven entrainment of warm thermocline waters, when sea-ice motion is anomalously fast (Fig. 2c).

For the same atmospheric forcing, the first model year shows warmer deviations from freezing temperature than the second model year because entrainment taps a heat source (below the mixed layer) that is not replenished in our simulation. At the start of the first year, integrated ocean heat content (relative to the freezing temperature) in a 50 m thick layer below the base of the mixed layer is about $0.5 \times 10^7 \text{ J m}^{-3}$ more than at the start of the second year of the simulation. If all of the excess thermocline heat in the first year is used to melt or slow the growth of sea ice, this amounts to about 90 cm (see e.g. the calculations in Timmermans, 2015). Of course some fraction of this heat is likely lost to the atmosphere, so this thickness estimate represents an upper bound. We observe about 50–70 cm more sea-ice thickness loss in the first year than in the second year, which is generally in agreement with the interannual difference in sea-ice decay resulting from the additional ocean heat source in the first year.

3.3. Buoyancy and heat fluxes at the ice-ocean interface

It is instructive to set mixed-layer properties in context with buoyancy fluxes J_b [$\text{m}^2 \text{ s}^{-3}$] at the ice-ocean interface, computed as contributions from heat fluxes J_Q [W m^{-2}] and salinity fluxes J_s [$\text{kg m}^{-2} \text{ s}^{-1}$]:

$$J_b = -\frac{g}{\rho_0} \left[\frac{\alpha}{c_p} J_Q + \beta J_s \right], \quad (1)$$

where $\alpha = -(1/\rho_0)(\partial\rho/\partial T)_{S,p}$ is the thermal expansion coefficient (ρ_0 is a reference density), $\beta = (1/\rho_0)(\partial\rho/\partial S)_{T,p}$ is the haline contraction coefficient and c_p is specific heat capacity of sea water ($c_p = 4.1 \times 10^3 \text{ J kg}^{-1} \text{ }^\circ\text{C}^{-1}$); for typical surface-ocean temperature and salinity values, $\alpha \approx 3 \times 10^{-5} \text{ }^\circ\text{C}^{-1}$, and $\beta \approx 8 \times 10^{-4}$. For these polar conditions, buoyancy fluxes are dominated by salinity fluxes (Fig. 4a).

Time series of J_b indicate small consistently negative fluxes during the winter ice-growth season associated with release of dense

brine into the surface ocean. J_b becomes positive during the summer melt season when ice melt drives the release of fresh waters into the surface ocean (Fig. 4a). Over an annual cycle of typical Arctic forcing under the multi-year sea-ice pack, J_b ranges between maximum positive values of about $5 \times 10^{-9} \text{ m}^2 \text{ s}^{-3}$ during summer and $-0.5 \times 10^{-9} \text{ m}^2 \text{ s}^{-3}$ during winter. These values are at least an order of magnitude smaller than buoyancy fluxes (in both summer and winter) typical of midlatitude basins: e.g., $J_b \sim \mathcal{O}(10^{-7}) \text{ m}^2 \text{ s}^{-3}$ (Gulf Stream jet; Thomas et al. (2008)), and $J_b \sim \mathcal{O}(10^{-8}) \text{ m}^2 \text{ s}^{-3}$ (California Current; Brainerd and Gregg (1993)). Although winter months are characterized by brine release and convective instabilities, the presence of sea ice throughout the simulation limits sea-ice growth by conduction, and therefore strong buoyancy fluxes. The relevance of this to the observed dynamics will be discussed in Section 4.

The heat flux at the base of the ice J_Q is the sum of the conductive heat flux arising from atmospheric heat transfer, and the turbulent ocean-to-ice heat flux $J_{Q_{oi}}$ (Fig. 4b). In summer, the latter is large due to solar warming through thin ice and open water areas. In both seasons enhanced $J_{Q_{oi}}$ may be driven by upper-ocean dynamics that lead to entrainment of warm water from below the mixed-layer base. This entrainment takes place when ice-ocean shear or convection is strong, and may arise by SM processes associated with enhanced vertical and horizontal flows. Entrainment events (and increased $J_{Q_{oi}}$) driven by enhanced ice-ocean stress are notable in December and April/May.

The magnitude of the turbulent ocean-to-ice heat flux $J_{Q_{oi}}$ [W m^{-2}] is estimated by the following parameterization (Maykut and McPhee, 1995),

$$J_{Q_{oi}} = \rho_0 c_h c_p u^* (T - T_f), \quad (2)$$

where $\rho_0 = 1000 \text{ kg m}^{-3}$ is a reference seawater density, $c_h \approx 0.006$ is a heat transfer coefficient and u^* is the magnitude of the friction velocity at the ice-ocean interface (computed as $u^* = \sqrt{|\boldsymbol{\tau}_i|/\rho_0}$, where $\boldsymbol{\tau}_i = (\tau_i^x, \tau_i^y)$ is the ice-ocean stress).

$J_{Q_{oi}}$ presents a seasonal cycle (Fig. 4b) with consistently larger values during summer months (domain-averaged values of \sim

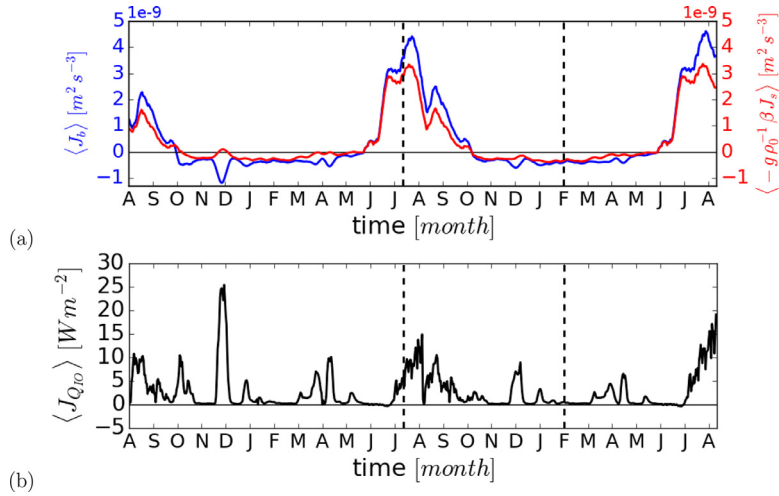


Fig. 4. (a) Time series of domain-averaged buoyancy flux J_b [m² s⁻³] (blue line, left axis) and salinity buoyancy flux $-\rho_0 g^{-1} \beta J_s$ [m² s⁻³] (red line, right axis) at the ice-ocean interface. Values are filtered with a Kaiser window of approximately 10 days (Kaiser and Kuo, 1966). (b) Time series of domain-averaged ocean-to-ice turbulent heat flux J_{Qo} [W m⁻²]. Values are unfiltered. In both (a) and (b), vertical dashed lines indicate representative summer and winter days. (For interpretation of the references to color in this figure legend, the reader is referred to the web version of this article.)

15 Wm⁻²) and minima of zero during the winter season with sporadic events of magnitude similar to the summer season associated with thermocline entrainment; this seasonal cycle is consistent with that documented by McPhee (2003) under sea ice in the vicinity of the north pole. During the events of increased ice-ocean shear (December and April/May), values of domain averaged J_{Qo} were found to compare in magnitude to the summer heat fluxes ($J_{Qo} \sim 10$ Wm⁻²); reduced sea-ice growth rates in both December and April/May (Fig. 2a) may be attributed to the enhanced ocean-to-ice heat fluxes. The first model year shows larger winter heat fluxes (e.g., note the event in December of the first year, Fig. 4b) than the second model year because the sub-mixed layer heat source is not replenished in our simulation, as noted earlier. In Section 4.5, we examine submesoscale-driven ocean heat fluxes.

4. Characterizing upper-ocean dynamics

In this section, we describe the main mechanisms driving upper-ocean dynamics. We begin by characterizing the dynamics of the flow below the mixed layer, on the 50 m depth level in the halocline. We proceed by describing the dynamics in the mixed layer (at 2 m depth in summer and 20 m depth in winter). For both the interior halocline and the mixed layer, we distinguish between seasons, and analyze representative summer and winter days. Finally, dynamics in the mixed layer are further analyzed with respect to SM flows, and we examine two different cases presenting SM activity.

Upper-ocean dynamics are diagnosed in time-depth series of Rossby number $Ro = \zeta / f_0$, vertical velocity w , and Richardson number $Ri = N^2 / |\partial \mathbf{u} / \partial z|^2$, where $\mathbf{u} = (u, v)$ is horizontal velocity, $\zeta = \partial v / \partial x - \partial u / \partial y$ is the vertical relative vorticity, $f_0 = 1.4 \times 10^{-4}$ s⁻¹ is the Coriolis parameter at 75°N, and $N^2 = -\frac{g}{\rho_0} \frac{\partial \rho}{\partial z}$ is the buoyancy frequency (Fig. 5). These diagnostics are chosen in order to highlight the nature of SM features, which are characterized by $\mathcal{O}(1)$ Rossby numbers, associated with enhanced vertical velocities, and develop in regions of weak stratification.

Throughout the year, Ro shows a gradient between small values in the mixed layer and larger values in the interior halocline depths (Fig. 5a). The depth dependence of Ro is consistent with much larger horizontal density gradients in the interior compared to the mixed layer (i.e., stronger baroclinic activity in the interior). Larger Ro in the remnant winter mixed layer may be associated

with stretching/squashing of this weakly-stratified layer (by perturbations in the mixed layer and underlying more stratified water column) and limited influence from damping by surface stresses. Larger Ro in the mixed layer are found in a few sporadic events, the strongest of which is in February/March. These events are associated with relatively long periods of negligible ice drift (i.e., weaker ice-ocean shear, Fig. 2c) which corresponds to increased vertical and lateral density gradients within the mixed layer (weak surface stresses allow for a weakening of the vertical stratification across the base of the mixed layer), and evidently increased baroclinic activity there. Larger standard deviations in BLD at this time (Fig. 2d) indicate spatial inhomogeneity, consistent with baroclinic flows in the mixed layer. A detailed description of the February/March episode is given in Section 4.4.

Resolved vertical velocities in the mixed layer are weak throughout the simulation (Fig. 5b). Instances where mixed-layer w deviates from zero are associated with the events of increased baroclinic flows, and enhanced vertical ageostrophic circulation across density fronts, during times of small sea-ice drift speeds. Ri is smallest in the mixed layer, with the smallest values near the ice-ocean interface corresponding to the largest vertical shear (Fig. 5c). Lower shear and stronger stratification give rise to larger Ri and w in the mixed layer during the February/March events described above. The mixed layer and the interior present distinctively different dynamics, and it is clarifying to compare these, drawing insights from comparison to upper-ocean dynamics in the midlatitudes. We consider two model days representative of summer conditions (corresponding to the middle of the melt period, Fig. 5, left vertical dashed line) and winter conditions (corresponding to the middle of the ice-growth period and maximum BLD, Fig. 5, right vertical dashed line). The representative summer day is July 11th of the first year of the integration, and the representative winter day is February 1st of the second year. We quantify the dynamics in the model by considering the horizontal momentum balance

$$\frac{\partial \mathbf{u}}{\partial t} + \mathbf{u} \nabla_h \mathbf{u} + f_0 \hat{k} \times \mathbf{u} + \rho_0^{-1} \nabla_h p - \frac{\partial}{\partial z} A_z \frac{\partial \mathbf{u}}{\partial z} - \rho_0^{-1} \frac{\partial \boldsymbol{\tau}_i}{\partial z} = 0, \quad (3)$$

where A_z is vertical viscosity as computed by KPP, p is pressure, subscript h denotes horizontal derivatives, and $\boldsymbol{\tau}_i$ is the ice-ocean stress (only non-zero in the first model layer). Lateral mixing is negligible.

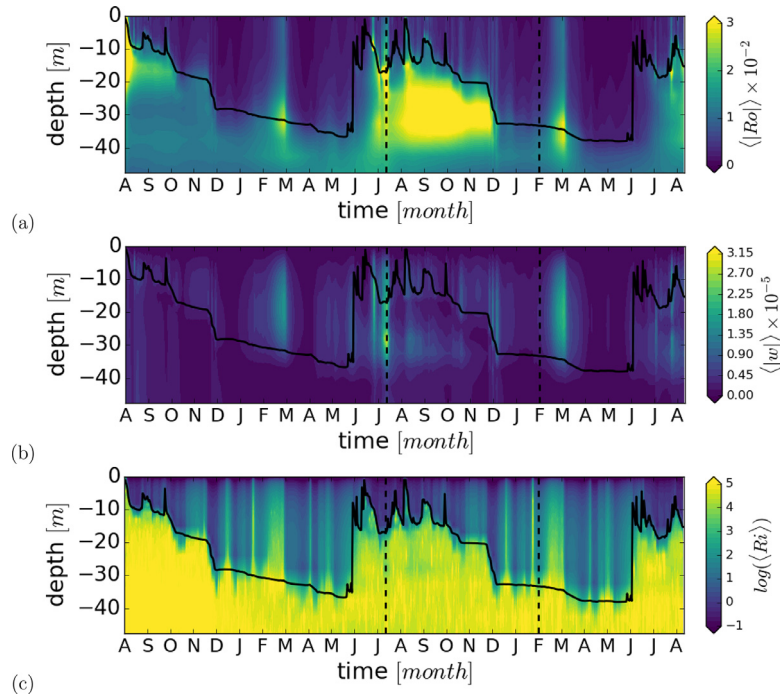


Fig. 5. Horizontally averaged time-depth sections of (a) Rossby number $Ro = \zeta/f_0$, (b) vertical velocity w [m s^{-1}], and (c) Richardson number Ri . The black contour indicates the BLD and the vertical dashed lines mark representative summer and winter days.

4.1. Dynamics in the interior

Results are presented for representative summer and winter days; the flow fields exhibited in the two selected days are common throughout the respective seasons. On both representative winter and summer days, the interior (halocline) is characterized by a range of eddies and filaments consistent with baroclinic instability (Fig. 6). To explore the main dynamical balances in the interior, we compute the dominant terms in the horizontal momentum balance (3) (Fig. 7) along segments at 50 m depth across typical eddies for each of the summer and winter days (black lines in Fig. 6).

During the representative summer day, the main balance through a typical eddy feature is geostrophic, with some time dependence (Fig. 7a,b: x and y components, respectively). The latter becomes relatively more important outside the eddy, where the azimuthal flow weakens, and in the core of the eddy where Coriolis and pressure gradient forces pass through zero. The time dependence indicates the presence of more rapidly evolving features such as internal waves. Enhanced internal wave activity is evident in fields of the horizontal density gradient $|\nabla_h \rho|$ and Ro in the interior in summer (Fig. 6a,b). Similar events have been tracked in observations beneath sea ice during the summer (e.g., Dosser et al., 2014); the details of internal wave dynamics will be further analyzed in the next section.

During the representative winter day, the balance through a typical eddy is predominantly geostrophic (Fig. 7c and d, x and y components respectively) with only weak internal wave activity. Winter interior $|\nabla_h \rho|$ and Ro (Fig. 6c and d) fields are consistent with weak quasi-geostrophic dynamics typically found in the stratified interior of temperate oceans (Phillips, 1963; Charney, 1971; Rhines, 1979).

4.2. Dynamics in the mixed layer

4.2.1. Summer

The typical summer day indicates a mixed layer that is characterized by density gradients associated with lateral variations in surface freshwater fluxes as a result of ice melt (Fig. 8a). Although

there are regions of enhanced $|\nabla_h \rho|$, these maxima ($|\nabla_h \rho| \sim \mathcal{O}(10^{-8}) \text{ kg m}^{-4}$) are significantly smaller than those found in typical SM fronts in the mid-latitudes ($|\nabla_h \rho| \sim \mathcal{O}(10^{-5}) \text{ kg m}^{-4}$, (Capet et al., 2008d)).

The summer mixed layer is generally characterized by small-scale features developing in the form of organized structures very near the surface; a segment (indicated by a black line in Fig. 8a and b) is chosen to cross such a feature in the summer mixed layer. The momentum balance along the segment is a dominant Ekman balance at 2 m depth (Fig. 9a, x -component). This balance holds throughout most of the year in the surface layer subject to persistent ice-ocean stresses (see e.g., Cole et al., 2013). In the y -component (Fig. 9b) on the representative summer day in the mixed layer, we see an exception to this main balance with all terms (Coriolis, pressure gradient and friction) having similar magnitude.

To understand the processes leading to such dynamics, we examine a time series of the momentum balance terms (Fig. 10a and b: x and y component, respectively) averaged over a small region around the segment (shown in Fig. 8a and b). The Ekman balance generally dominates both the x and y components with a change in sign of the Coriolis and vertical mixing terms when the ice drift changes direction (τ_i^x or τ_i^y changes sign). A delay of about one inertial period is observed in the ocean response to the change in ice-ocean stress.

On the representative summer day (marked by the vertical black line in Fig. 10a and b), it is clear that a temporary weakening of surface stress results in rapid decay of vertical mixing in the y -direction and a temporary loss of Ekman balance (Fig. 10b). The Ekman balance is absent (Fig. 9b), with the Coriolis term partially balanced by v_t driving near-inertial oscillations (see e.g., D’Asaro, 1985). The Ekman balance is restored soon after τ_i^y increases from zero. A similar event can be identified in the x -component time series around day 6/28 (Fig. 10a).

Ice-ocean stress is highly variable in time, although it does not exhibit any apparent seasonal cycle (not shown). For the same wind energy input, stronger inertial flows are generated in shallower mixed layers (see e.g., D’Asaro, 1985); during the

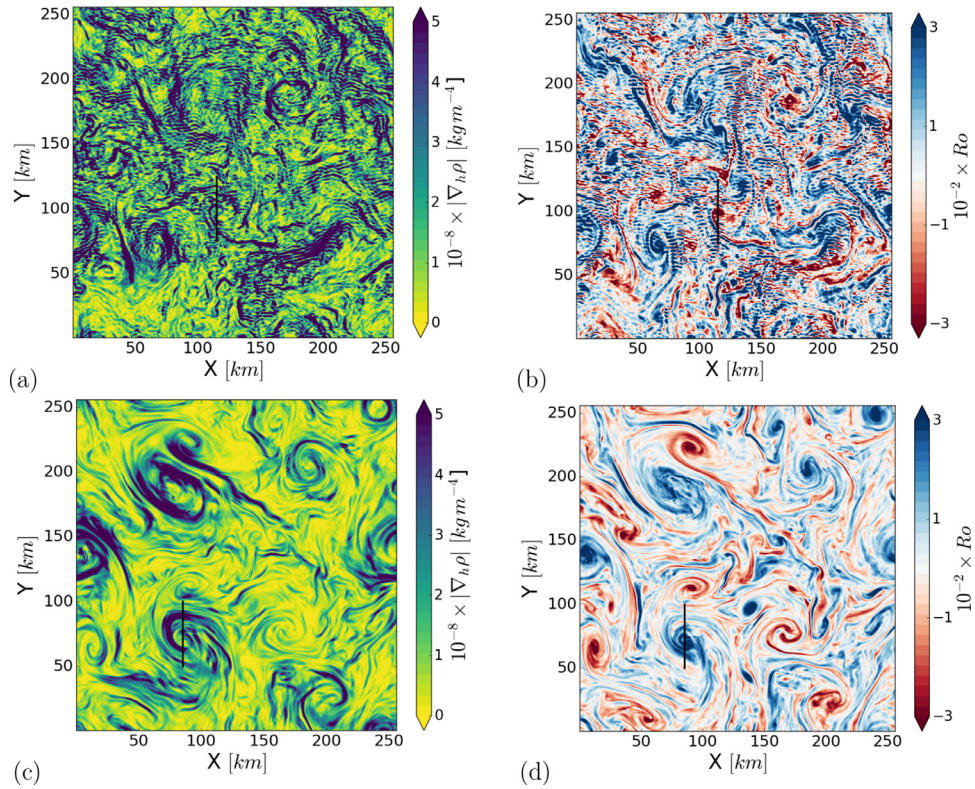


Fig. 6. Horizontal density gradient magnitude $|\nabla_h \rho|$ [kg m^{-4}] at 50 m depth (the interior) for the representative (a) summer and (c) winter days. Ro at 50 m depth for (b) summer and (d) winter days. The black lines represent the segments along which the momentum balance terms are computed.

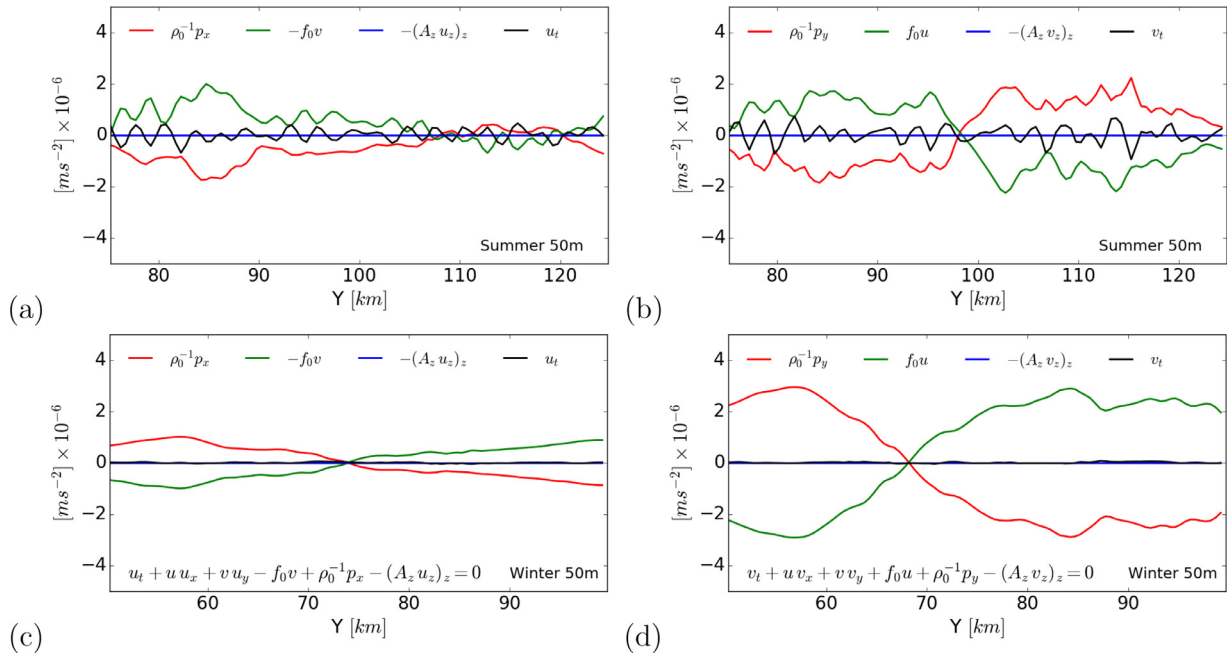


Fig. 7. Terms in the (a) x-momentum balance and (b) y-momentum balance for the summer day along the segment at $X = 135$ km at 50 m depth. Terms in the (c) x-momentum and (d) y-momentum balance for the winter day along the segment at $X = 85$ km at 50 m depth. The two segments along which momentum terms are computed are shown by the black lines in Fig. 6c and d. The bottom panels show the two horizontal momentum equations. The inertial terms (not plotted) are negligible.

summer season characterized by thin mixed layers, the generation of energetic near-inertial waves is more prevalent. Near-inertial waves can propagate to depth resulting in the clear internal wave signature observed in summer in the interior (Fig. 6a and b).

Hovmöller diagrams of vertical velocity (not shown) confirm the propagation of internal waves from their origins near the surface to the interior (see e.g., Rainville and Woodgate, 2009; Dosser et al., 2014). Note that it is possible that results would be different in a non-hydrostatic model (Magaldi and Haine, 2012).

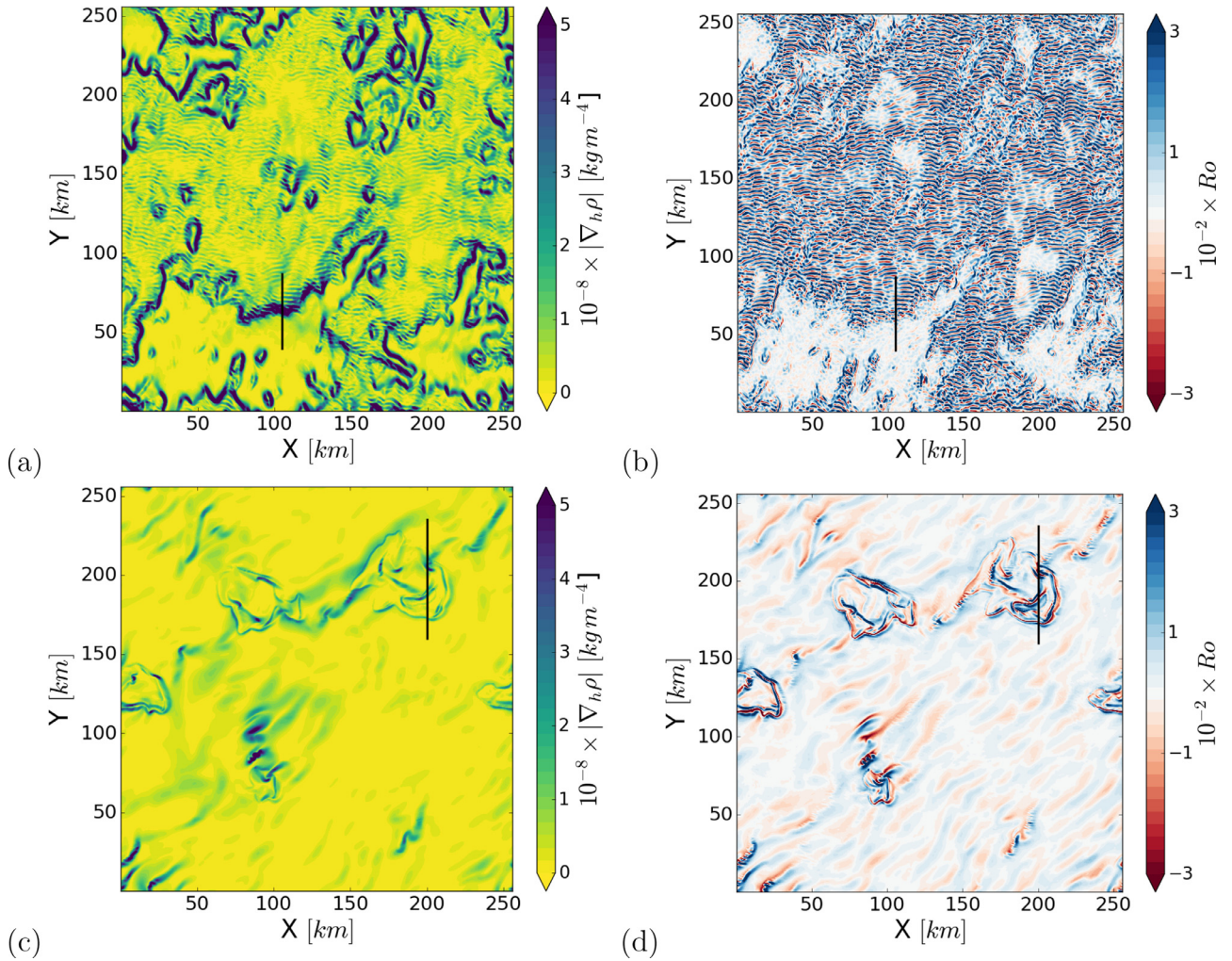


Fig. 8. Horizontal density gradient $|\nabla_h \rho|$ [kg m^{-4}] for (a) summer (at 2 m depth) and (c) winter (at 22 m depth) days. Ro for (b) summer (at 2 m depth) and (d) winter (at 22 m depth) days. Different depths were chosen between summer and winter in order to show diagnostics around the mid-depth of the mixed layer for both days. The black lines represent the segments along which the momentum balance terms are computed.

4.2.2. Winter

The representative winter day exhibits elongated structures in the mixed layer, with generally larger magnitude Ro and smaller $|\nabla_h \rho|$ compared to the representative summer day (Fig. 8c and d). Larger values of $|\nabla_h \rho|$ are associated with the boundaries of regions of enhanced vertical mixing (Fig. 8c). These structures are the large-scale signature of convective cells associated with brine rejection during ice growth.

The relatively coarse horizontal resolution, as well as the hydrostatic nature of the model, do not allow for the resolution of individual brine plumes; nevertheless, convection parameterized by KPP as enhanced vertical viscosity generates regions of relatively salty water adjacent to relatively fresh water. Jones and Marshall (1993) and Legg et al. (1998) put forward the possibility of similar features developing along the large scale signature of convective cells in ocean general circulation models (see also Gawarkiewicz and Chapman (1995) who modeled these processes in regions of sustained sea-ice growth).

The momentum balance (3) along a winter segment (denoted by the black line in Fig. 8c and d) in the mixed layer through one of the enhanced $|\nabla_h \rho|$ structures is a steady Coriolis, vertical mixing, pressure gradient balance (Fig. 9c–f). The horizontal flow field in the mixed layer shows an Ekman spiral forced by ice-ocean stress that is oriented primarily along the y -direction. The

Ekman layer thickness scales as $\sqrt{2A_z/f_0} \approx 12$ m. At 2 m depth, the Ekman balance dominates (Fig. 9c and d), while at 22 m depth (Fig. 9e and f), the pressure gradient force becomes more important, vertical mixing weakens and the flow is in turbulent thermal wind balance (see e.g., Gula et al., 2014; Brannigan et al., 2015). Near the surface at 2 m depth, velocities are larger in magnitude than below the Ekman layer, with most of the magnitude difference in u , and mainly only a change in sign of v (not shown). Below the Ekman boundary layer, away from the dominant influence of ice-ocean stress, the mixed-layer flow is characterized by larger magnitude Ro .

4.2.3. Frontal tendency and vertical buoyancy fluxes

In numerical simulations of ice-free oceans, it is common to observe values of Ro and w in the mixed layer that are a couple of orders of magnitude larger than in our simulation under sea ice (e.g., Boccaletti et al., 2007). These higher values of Ro and vertical velocity in the temperate oceans are typical of the winter season when deep mixed layers ($\mathcal{O}(100)$ m deep) develop in coincidence with large horizontal density gradients ($|\nabla_h \rho| \sim 10^{-4}$ kg m^{-4} ; Capet et al. (2008c)).

In the midlatitudes an energetic SM flow field can be attributed to the intensification of horizontal density gradients, a process known as frontogenesis (Hoskins, 1982), and the formation of baro-

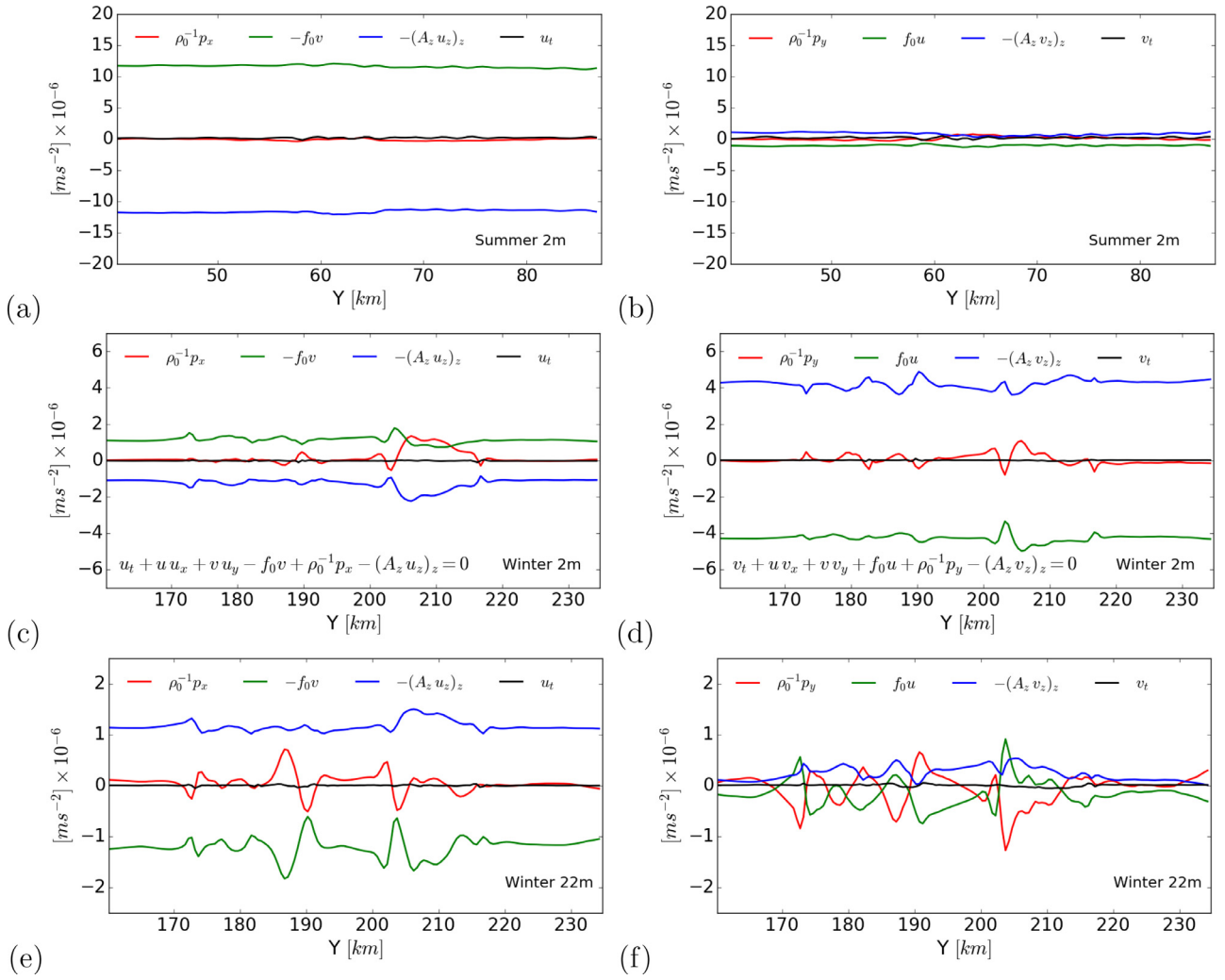


Fig. 9. Terms in the (a) x -momentum balance and (b) y -momentum balance for the summer day for a segment along $X = 105$ km at 2 m depth, and for (c,e) x -momentum balance and (d,f) y -momentum balance for the winter day for a segment along $X = 200$ km at (c,d) 2 m and (e,f) 22 m depth. The two segments along which momentum terms are computed are shown by the black lines in Fig. 8c and d, for $X = 105$ km and 200 km, respectively. Panels (c) and (d) show the two horizontal momentum equations. The inertial terms (not plotted) are negligible.

clinic/symmetric instabilities (e.g., Boccaletti et al., 2007; Capet et al., 2008b; Mensa et al., 2013; Thomas et al., 2013; Brannigan et al., 2015). The frontal tendency $F_T = \frac{D|\nabla_h \rho|^2}{Dt}$ [$\text{kg}^2 \text{m}^{-8} \text{s}^{-1}$] (Hoskins, 1982), is a metric for frontogenesis. At the mesoscale, F_T is primarily driven by horizontal advection; following Capet et al. (2008d), we use this form of the frontal tendency: $F = \mathbf{Q} \cdot \nabla_h \rho$, where $\mathbf{Q} = -(\partial_x u \partial_x \rho + \partial_x v \partial_y \rho, \partial_y u \partial_x \rho + \partial_y v \partial_y \rho)$. On both the representative winter and summer days, F takes positive and negative values in similar magnitude (Fig. 11a). Maximum values of $|F| \sim 7.5 \times 10^{-16} \text{ kg}^2 \text{m}^{-8} \text{ s}^{-1}$ found during the summer (winter maxima at 22 m are $|F| \sim 4.5 \times 10^{-16} \text{ kg}^2 \text{m}^{-8} \text{ s}^{-1}$, with similar values at 2 m depth in winter) are much smaller than typical values in temperate mixed layers: typical values for the Gulf Stream and California Current can be as large as $|F| \sim 10^{-13} \text{ kg}^2 \text{m}^{-8} \text{ s}^{-1}$ (Capet et al., 2008a; Mensa et al., 2013). Moreover, when active frontogenesis is observed, F presents a clear positive skewness. In our simulation, skewness is nearly zero in both summer and winter (Fig. 11a). The absence of strong frontal tendency and the presence of regions of positive and negative F on both sides of fronts is a sign that density gradients do not intensify and submesoscale instabilities do not develop.

The presence (or absence) of SM activity is diagnosed via vertical buoyancy fluxes $w'b'$ (taken here as anomalies with respect to a 10-day mean) in which mixed layer instabilities and fronts release available potential energy, restratifying the mixed layer and driving positive buoyancy fluxes. As expected, associated with weak frontogenesis, we observe small values of $w'b'$; nominally larger $w'b'$ are observed in winter, coincident with the boundaries of convective regions. Overall, values of $w'b'$ range between $\pm 10^{-9} \text{ m}^2 \text{ s}^{-3}$ during summer and $\pm 10^{-8} \text{ m}^2 \text{ s}^{-3}$ in winter, significantly smaller than values typical of the midlatitudes where $w'b' \sim \mathcal{O}(10^{-7}) \text{ m}^2 \text{ s}^{-3}$ in the winter Gulf Stream (Mensa et al., 2013), in the winter Kuroshio Current (Sasaki et al., 2014) in the summer California Current (Capet et al., 2008d) and winter Argentinian shelf (Capet et al., 2008b).

4.3. Kinetic energy spectra

Kinetic energy (KE) spectra computed in the mixed layer and interior for both seasons provide further evidence for the different seasonal characteristics of the flow (Fig. 11b). In winter, horizontal wavenumber (k) spectra in the interior have spectral slopes around k^{-3} for most of the range of sampled wavenumbers, an indication of the forward enstrophy cascade associated with quasi-

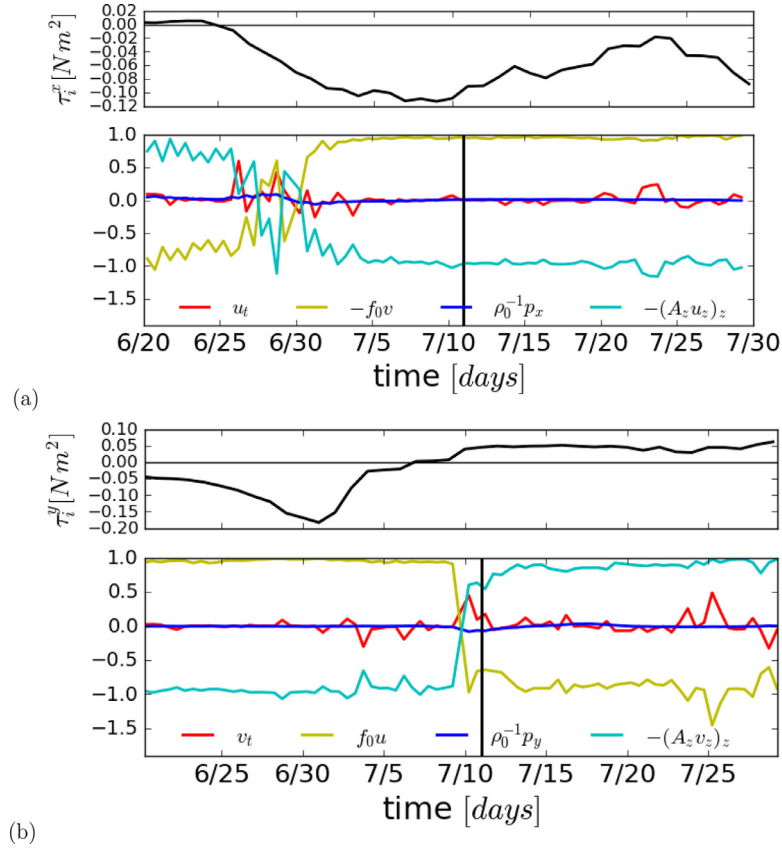


Fig. 10. Time series (around the representative summer day) of the terms in the (a) x -momentum balance (lower panel) and b) y -momentum balance (lower panel) averaged over the domain at 2 m depth. All plotted quantities are normalized with respect to the maximum term at each time. The upper panels in (a) and (b) show time series of the averaged ice-ocean stress τ_i (for the x - and y -components τ_i^x and τ_i^y , respectively). Black vertical lines in the lower panels indicate the summer day. The inertial terms in the momentum balance (not plotted) are negligible.

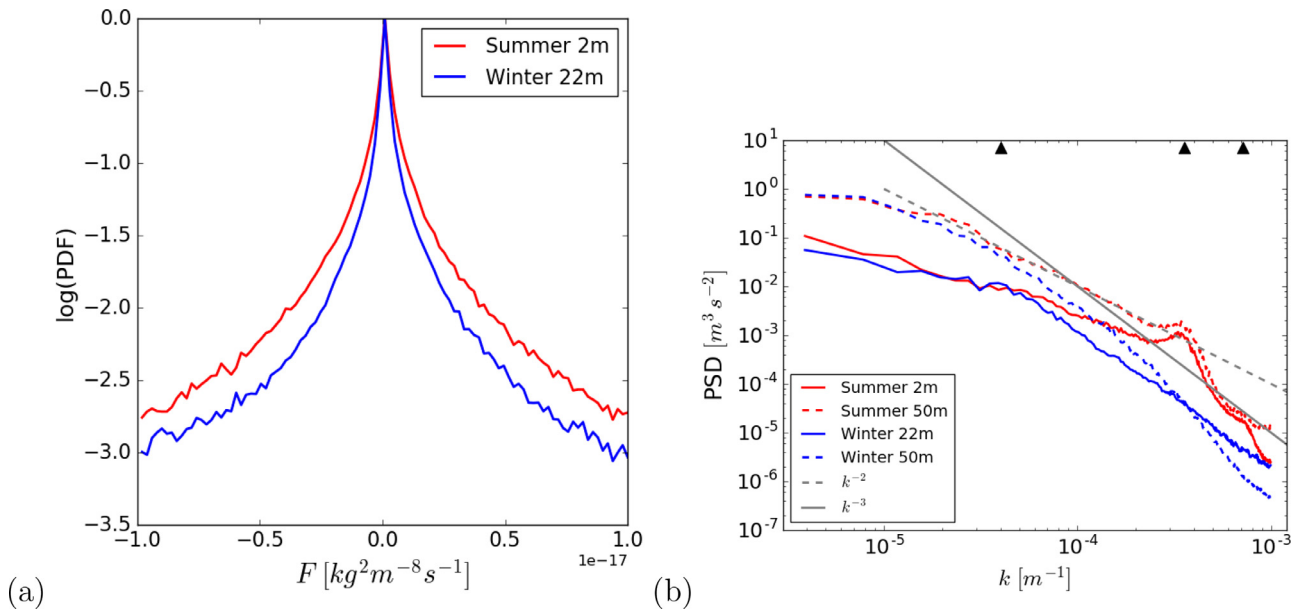


Fig. 11. (a) PDF of frontal tendency F [$\text{kg}^2 \text{m}^{-8} \text{s}^{-1}$] computed for representative (red) summer (at 2 m depth) and (blue) winter (at 22 m depth) days for all points in the domain. (b) Horizontal wavenumber (k) spectra of kinetic energy (KE) for the representative winter and summer days at 2 m, 22 m and 50 m depth. The grey lines indicate a k^{-2} (dashed) and k^{-3} (solid) slope. Spectra are computed for a single day along X-points, and then along Y-points. The resulting spectra are then averaged across wavenumbers. The black triangles correspond, from left to right, to wavelengths of 25 km, 2.8 km and 1.4 km. (For interpretation of the references to color in this figure legend, the reader is referred to the web version of this article.)

geostrophic turbulence. In summer, the horizontal wavenumber spectra of KE in the interior are shallower than in winter (closer to a k^{-2} slope), consistent with enhanced internal wave energy in summer (c.f., Fig. 6). Summer spectra are also characterized by an injection of energy at the scale of the near-inertial oscillations (wavelength ~ 3 km) with a secondary peak (only partially resolved) at about ~ 1.5 km (corresponding to the two right triangles, Fig. 11b). Energy is injected on near-inertial scales and transferred to surrounding scales via wave-wave interaction resulting in a k^{-2} slope (e.g., McComas and Bretherton, 1977). Energy travels from near the surface to depth in wave packets characterized by a group velocity of ~ 80 m day $^{-1}$ (measured from Hovmöller diagrams) and a corresponding vertical wavelength of ~ 15 m. These values are consistent with observations of near-inertial waves in other ocean basins (Alford et al., 2016).

In the mixed layer in both seasons (solid lines in Fig. 11b) spectra are relatively flat at scales larger than about 25 km (left triangle in Fig. 11b), indicative of a weak mesoscale flow field in the mixed layer. At smaller horizontal scales, winter wavenumber spectra transition to a steeper slope (closer to k^{-3} slope), consistent with the weak dynamics of the winter mixed layer (in agreement with Timmermans et al., 2012). On the other hand, summer wavenumber spectra remain shallow (closer to k^{-2} slope) for a broader range of scales, again consistent with enhanced internal wave energy in summer.

4.4. Sporadic generation of submesoscale features

The mixed layer has been shown to present weak SM activity during both summer and winter. Exceptions to this are observed during events where larger $|\nabla_h \rho|$ coincide with weaker ice-ocean stresses, and baroclinic instability is uninhibited. We investigate two such cases: one in which lateral density gradients are generated by horizontally inhomogeneous convection that ensues where there are linear openings (leads) in the sea-ice pack, and another in which lateral density gradients are generated by convection resulting from inhomogeneous sea-ice growth over the domain. In both cases, instabilities are favored by the temporary weakening of sea-ice motion (and therefore, weaker ice-ocean shear).

In all seasons, it is not uncommon for the ice pack to develop cracks, or leads, exposing the ocean below to direct atmospheric fluxes. Within a wintertime lead, sea-ice grows rapidly from the exposed ocean, and the result is a strong negative buoyancy flux due to brine rejection. In one such event, a ~ 20 km long lead, about a few kilometers wide, appeared in November (Fig. 12a), and remained open for several days resulting in a persistent negative buoyancy flux at the ocean surface. The surface buoyancy flux during this event was ~ 20 times larger than fluxes under the adjacent ice cover, which were $J_b \sim -0.1 \times 10^{-9}$ m 2 s $^{-3}$. As the ice pack drifted, the large buoyancy flux resulted in a region of increased salinity in the wake of the lead. The associated enhanced $|\nabla_h \rho|$ and the formation of baroclinic instabilities lead to enhanced values of Ro ; at mid-depth in the mixed layer Ro attained values of ~ 0.3 (Fig. 12b), closer to those associated with SM in the midlatitudes. Vertical velocities in the developing flow features ($|w| \sim 4 \times 10^{-4}$ m s $^{-1}$) were also significantly larger than in the surrounding regions. The total duration of the event was about 20 days, from the time the lead opened to complete dissipation of the instability, which took place rapidly as soon as ice-drift speed increased.

A similar event associated with stronger SM features is that observed in the time series of Ro , w and Ri in February (Fig. 5). Unlike the previous case, in which intensified horizontal density/salinity gradients were present only along the wake of a lead, increased $|Ro|$ were observed over a broad swath of the domain where ice growth was intensified under thinner sea ice compared to else-

where in the domain (Fig. 12d). Lateral salinity gradients and Ro at 17 m depth (the mid-depth of the mixed layer) were associated with lateral density gradients in the proximity of convective cells and the instabilities that tend to form along these regions (Fig. 12c and d). Instabilities develop maximum vertical velocities ($|w| \sim 5 \times 10^{-4}$ m s $^{-1}$) that are comparable to midlatitude values. The two examples described above indicate that instabilities develop whenever ice-ocean stresses are weaker (mixing is reduced) and convection is enhanced. Several other similar events, although having somewhat weaker flows, are observed throughout the winter during periods of slow ice drift in the proximity of lateral density gradients set up by laterally inhomogeneous ice growth. The impact of these SM flows on ocean-to-ice heat fluxes will be examined next.

4.5. Ocean-to-ice heat fluxes in the presence of submesoscales

The two cases described above are characterized by the initial generation of convective regions with a locally deeper mixed layer followed by the rapid development of ageostrophic features via baroclinic instabilities and a final restratification phase (upon slumping of the lateral front). In each case, convective cells are surrounded by flows undergoing active frontogenesis with vertical velocities developing across density fronts. Enhanced vertical velocities at the boundaries of cold-salty parcels give rise to entrainment of warm waters below the mixed layer, leading to enhanced $J_{Q_{10}}$ with local values up to 5 W m $^{-2}$.

In both examples, as time progresses, baroclinic instabilities at the boundaries of the convecting regions are inferred from active SM; corresponding enhanced vertical velocities continue the sub-mixed layer entrainment, driving values of $J_{Q_{10}} \sim 0.4$ W m $^{-2}$. These are weaker fluxes than those associated with the primary convective parcel, although not insignificant.

During the restratification phase, enhanced ocean-to-ice heat fluxes associated with the convecting parcel and related instabilities return to near zero. The restratification is associated with a rapid and significant shoaling of the mixed layer, with BLD shoaling from 20 m before development of SM instabilities to ~ 10 m after restratification (a few days after the onset of the event). This may have important implications to the surface-ocean heat budget because the restratification insulates the surface layer in contact with sea ice from deeper ocean heat (see the discussion by Timmermans et al. (2012) related to observations of restratification). To quantify this effect, we compute that after the sea-ice lead event, mixed-layer potential energy decreases by approximately 20% during restratification by SM eddies. However, this is only a small fraction of the potential energy gain ($\sim 300\%$) during the successive shear-driven deepening (in agreement with analogous estimates by Timmermans et al. (2012) based on observations). At least in our numerical simulations under multi-year sea ice, we estimate that the restratification by SM instabilities has a negligible impact on the capacity of other mixing processes to drive ocean-to-ice heat fluxes.

During both SM events, frontogenesis and the formation of baroclinic instabilities are uninhibited whenever ice-ocean stress and mixing are reduced. In both instances, SM features are ultimately dissipated by the increase of vertical mixing as soon as ice drift increases. This phase is associated with large turbulent ocean-to-ice fluxes (~ 3 W m $^{-2}$). In general, $J_{Q_{10}}$ due to shear driven by sea-ice drift ($\mathcal{O}(1)$ W m $^{-2}$) is significantly larger than values attributed to SM flows ($\mathcal{O}(0.1)$ W m $^{-2}$). This is especially true with respect to the events of strong ice-ocean stress associated with rapid mixed-layer deepening described in the previous section ($J_{Q_{10}} \sim 10$ W m $^{-2}$ for the March/April and December events).

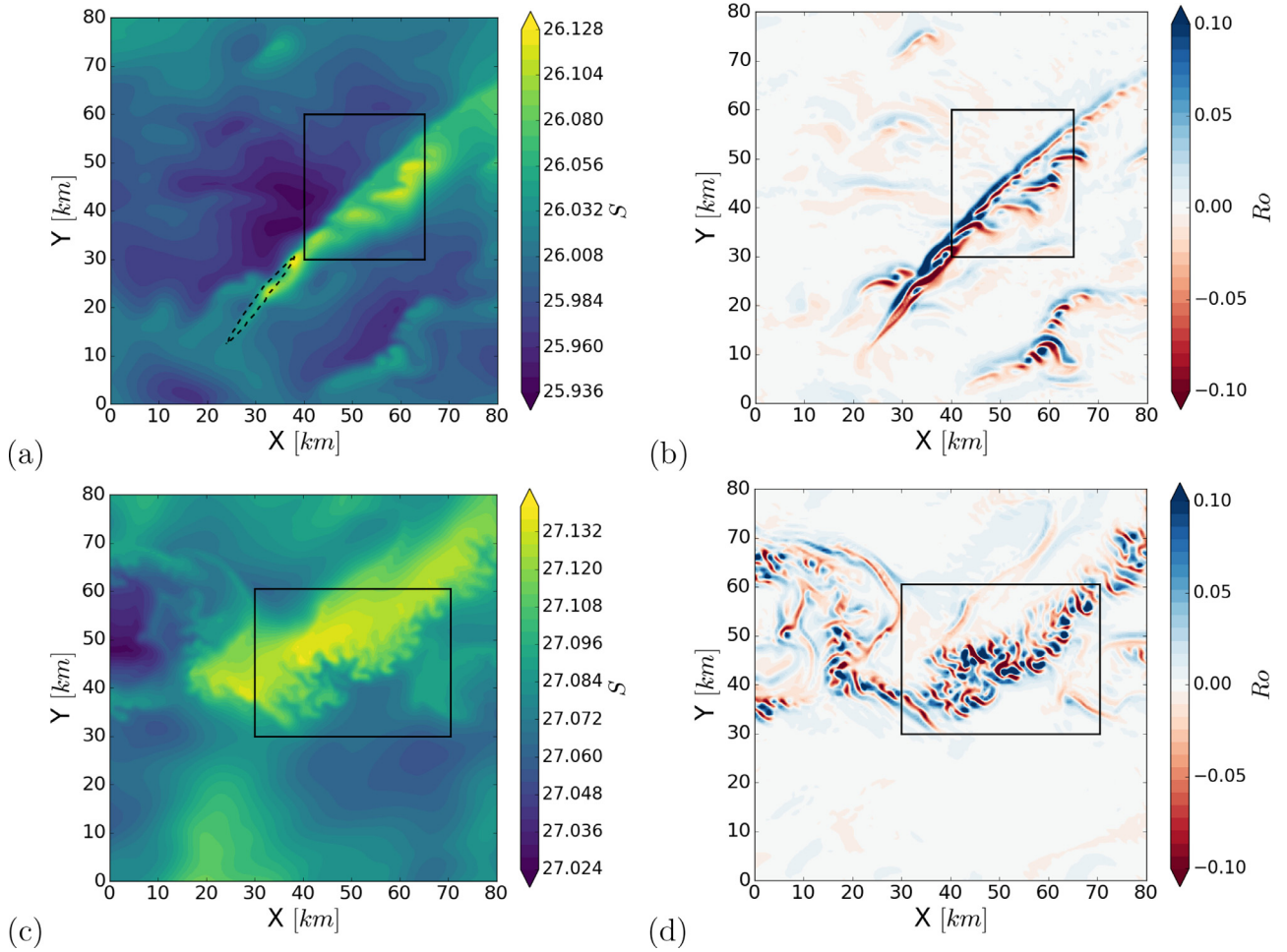


Fig. 12. Maps of (a) Salinity and (b) Ro for a region of the model domain at 11 m depth for November 5th (day 455 of the simulation). The black dashed line in (a) represents the 0.5 m ice thickness contour showing the position of the lead. (c) Salinity and (d) Ro at 17 m depth for February 15th (day 560 of the simulation). The black boxes delineate regions over which vertical buoyancy fluxes are computed and averaged (Fig. 13).

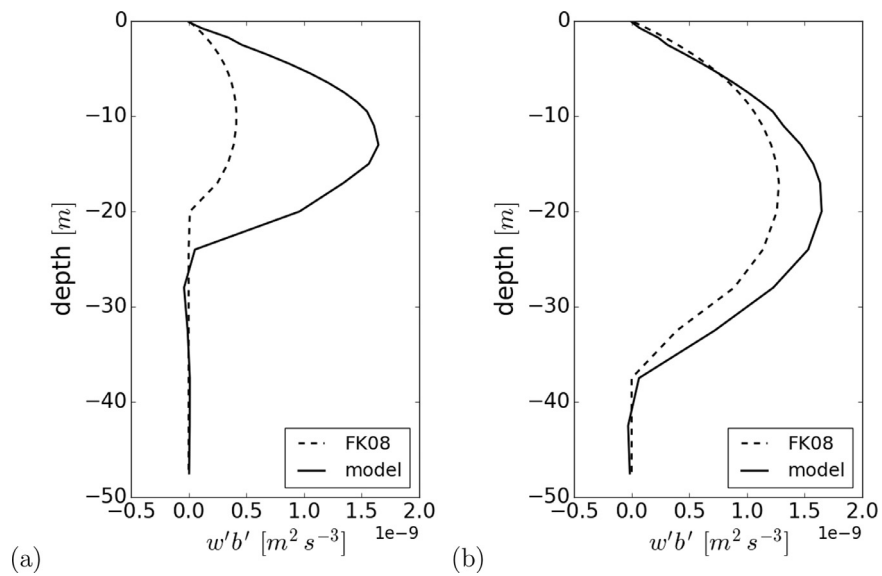


Fig. 13. Vertical buoyancy fluxes $w'b'$ [$m^2 s^{-3}$] computed directly from the model and from the FK08 parameterization (see text) for (a) the sea-ice lead shown in Fig. 12a and b and (b) the laterally varying convection shown in Fig. 12c and d. In each case, $w'b'$ values are averaged over the boxed areas in Fig. 12.

4.6. Evaluating a submesoscale parameterization

In light of the modeled KE wavenumber k spectra under sea ice, as well as the sporadic nature of SM features, the validity of existing SM parameterizations in this setting is not clear. SM parameterizations take the strength of the horizontal density gradient as the primary forcing of SM flows (which develop via baroclinic instability), and assume a KE spectrum that satisfies k^{-2} to relate unresolved to resolved scales (e.g., Fox-Kemper et al., 2008; Canuto and Dubovikov, 2010). Our simulations suggest, however, that SM features, when present, are associated with local convective processes. It remains to be understood how these conditions are represented by current parameterizations.

We have quantitatively tested the parametrization by Fox-Kemper et al. (2008) (hereafter FK08) for the four cases highlighted in the previous section: 1) typical summer (exhibiting enhanced internal wave activity); 2) typical winter (exhibiting convection and shear-driven mixing); 3) SM instabilities in the presence of laterally varying sea-ice growth; 4) SM instabilities in the presence of a lead. We compared modeled vertical buoyancy flux anomalies $w'b'$ to vertical buoyancy fluxes parameterized by FK08,

$$w'b'_{FK} = \frac{C_e |\nabla_h \bar{b}|^2 \overline{BLD}^2}{|f|} \mu(z), \quad (4)$$

where C_e is a constant ($C_e = 0.08$, (Fox-Kemper et al., 2008)) and $\mu(z)$ is a vertical structure function that decays to zero at the surface and at the base of the mixed layer (BLD). Overbars indicate averaging over a 10-day period, where the averaged field emulates that of a model that does not resolve SM. The parameterization (4) correctly produces negligible vertical buoyancy fluxes during typical summer and winter days (i.e., cases 1 and 2, with no SM flow field, Fig. 8). The lack of large-scale lateral density gradients in the winter case, and the shallow mixed layer of the summer case, result in weak parameterized and resolved buoyancy fluxes (not shown).

For cases 3) and 4), we compute profiles of $w'b'_{FK}$ (Fig. 8) through the upper ocean averaged over the area delineated by the boxes shown in Fig. 12; these regions were chosen to encompass an active SM field. For case 3), in which SM activity is associated with convective cells, the FK08 parameterization successfully reproduces the modeled buoyancy fluxes in their vicinity. This is consistent with the fact that SM flows are forced by the large-scale signature of convective cells, which is presumably resolved in coarse-resolution models. On the other hand, for case 4), the FK08 parameterization underestimates vertical buoyancy fluxes in the vicinity of a lead. In the case of the lead, the lateral density gradient (the source of SM activity) results from a relatively small-scale linear convective anomaly that is erased by our 10-day averaging, and not resolved by coarse-resolution models.

In sum, the FK08 parameterization is appropriate when SM features are generated by structures sufficiently large to be represented in coarse-resolution models (such as the convective cells described here). The parameterization cannot, however, predict vertical buoyancy fluxes associated with local processes such as density fronts generated by convection under ice leads. It remains to be examined how these SM features (unresolved in coarse-resolution models) may affect ocean dynamics and property transports on a basin scale.

5. Summary and discussion

An idealized high-resolution numerical simulation of the upper Arctic Ocean under sea ice, initialized by a surface density front with properties typical of observations (and subject to realistic atmospheric forcing), shows a seasonal sea ice cycle and upper-ocean properties consistent with observations. We have limited our

analysis to a permanently ice-covered regime. Seasonal variations in mixed-layer depth are smaller than generally observed in the midlatitude ice-free oceans, and range from a few meters in summer to ~ 35 m in winter. Sporadic deepening of the mixed layer is associated with shear-driven entrainment events which drive enhanced ocean-to-ice heat fluxes. Atmospheric fluxes are mediated by the presence of sea ice, resulting in generally slow sea-ice growth under thick ice and weak convective mixing, limiting the depth of the mixed layer.

Strong stratification across the base of the mixed layer, together with predominantly weak convective and shear-driven mixing, sets an effective separation between the interior (halocline) and the mixed layer. The interior presents slowly evolving mesoscale eddies with dynamics in quasi-geostrophic balance. In contrast with upper-ocean flows in the midlatitudes, these features do not influence mixed-layer dynamics and remain confined to the halocline. In our model setting under sea ice, mixed-layer dynamics are not driven by large-scale stirring by mesoscale flows in the interior. Weak SM flows are attributed to this lack of mesoscale stirring, and the impact of vertical mixing associated with ice-ocean stresses.

Throughout the year mixed-layer flows near the ice-ocean interface are in Ekman balance, which occasionally breaks down when ice-ocean stress weakens. In summer, characterized by strong stratification and shallow mixed layers, shifting wind-forcing events are associated with near-inertial oscillations. During winter, mixed-layer flows are typically in turbulent thermal wind balance with little evidence for energetic near-inertial oscillations. In both seasons, the dominance of vertical mixing in the mixed layer prevents frontogenesis which suppresses the generation of SM instabilities.

Sporadic instances of energetic SM features are observed where convective mixing (brine rejection) is enhanced under thin ice or when the ocean is exposed to the cold atmosphere (in a lead). Laterally inhomogeneous convective cells generate anomalously strong density gradients which undergo active frontogenesis and form baroclinic instabilities when ice-ocean stresses are weak. While SM flows drive entrainment of warm deep water, and corresponding local heat fluxes may be significant ($\sim 0.4 \text{ W m}^{-2}$), SM flows also drive mixed-layer restratification, which competes with mixed-layer deepening by convection and ice-ocean shear. Our simulations suggest, however, that this restratification has a negligible impact on the mixed-layer heat budget given the dominance of ice-ocean shear in driving mixing. In our multi-year sea-ice pack simulation, SM features are sparse and sporadic; their influence on the mixed-layer heat budget remains to be seen for settings in which they may be more prevalent.

The flow regime in the mixed layer is likely to be quite different in marginal ice zone regions, and in the presence of river inflows and large-scale gyre circulation and boundary currents. Future studies will examine the influence of varying sea-ice and oceanographic settings, particularly in context with Arctic Ocean observations. It remains to be understood how SM flows affect sea-ice thermodynamics for a variety of sea-ice conditions, and whether this can be effectively described by current numerical models. For example, numerical parameterizations of upper-ocean turbulence may significantly impact SM flow dynamics given the prominent role that vertical mixing has in our simulations (e.g., Goosse et al., 1999; Timmermann and Beckmann, 2004). Finally, we found the SM parameterization FK08 appropriately represents buoyancy fluxes associated with SM flows generated in conjunction with inhomogeneous ice growth across the model domain. On the other hand, in the case of convective anomalies on a smaller scale (e.g., sea-ice leads), the use of FK08 is not appropriate for parameterizing the effects of SM flows because their source fronts are not resolved. This points to the need for further study of parameteri-

zation schemes that can account for the effects of SM features in the vicinity of leads.

Acknowledgements

This research was made possible by a grant from The Gulf of Mexico Research Initiative as part of the Consortium for Advanced Research on Transport of Hydrocarbon in the Environment II. Computational resources were provided by the Center for Computational Sciences at the University of Miami. Model outputs, configurations, boundary and initial conditions are publicly available at doi:10.7266/N7GB2234. We thank three anonymous reviewers for their constructive comments.

References

- Adcroft, A., Campin, J., Dutkiewicz, S., Evangelinos, C., Ferreira, D., Forget, G., Fox-Kemper, B., Heimbach, P., Hill, C., Hill, E., et al., 2014. MITgcm User manual. MIT Department of EAPS Cambridge. http://mitgcm.org/public/r2_manual/latest/online_documents/manual.pdf.
- Alford, M.H., MacKinnon, J.A., Simmons, H.L., Nash, J.D., 2016. Near-inertial internal gravity waves in the ocean. *Ann. Rev. Mar. Sci.* 8, 95–123. doi:10.1146/annurev-marine-010814-015746.
- Backhaus, J.O., Kampf, J., 1999. Simulations of sub-mesoscale oceanic convection and ice-ocean interactions in the greenland sea. Deep - Sea Res. Part II - Topical Stud. Oceanogr. 46 (6–7), 1427–1455. doi:10.1016/S0967-0645(99)00029-6.
- Boccaletti, G., Ferrari, R., Fox-Kemper, B., 2007. Mixed layer instabilities and restratification. *J. Phys. Oceanogr.* 37 (9), 2228–2250. doi:10.1175/JPO3101.1.
- Brainerd, K., Gregg, M., 1993. Diurnal restratification and turbulence in the oceanic surface mixed layer: 1. observations. *J. Geophys. Res.* 98 (C12), 22645–22656.
- Brannigan, L., Marshall, D.P., Naveira-Garabato, A., George Nurser, A., 2015. The seasonal cycle of submesoscale flows. *Ocean Modell.* 92, 69–84. doi:10.1016/j.ocemod.2015.05.002.
- Budikova, D., 2009. Role of arctic sea ice in global atmospheric circulation: a review. *Glob. Planet. Change* 68 (3), 149–163. doi:10.1016/j.gloplacha.2009.04.001.
- Callies, J., Ferrari, R., Klymak, J.M., Gula, J., 2015. Seasonality in submesoscale turbulence. *Nat Commun.* 6, 6862. doi:10.1038/ncomms7862.
- Canuto, V.M., Dubovikov, M.S., 2010. Mixed layer sub-mesoscale parameterization - Part 1: derivation and assessment. *Ocean Sci.* 6 (3), 679–693. doi:10.5194/os-6-679-2010.
- Capet, X., Klein, P., Hua, B.L., Lapeyre, G., McWilliams, J.C., 2008a. Surface kinetic energy transfer in surface quasi-geostrophic flows. *J. Fluid Mech.* 604, 165–174. doi:10.1017/S0022112008001110.
- Capet, X., McWilliams, J.C., Molemaker, M.J., Shchepetkin, A.F., 2008b. Mesoscale to submesoscale transition in the california current system. part I: flow structure, eddy flux, and observational tests. *J. Phys. Oceanogr.* 38 (1), 29–43. doi:10.1175/2007JPO3671.1.
- Capet, X., McWilliams, J.C., Molemaker, M.J., Shchepetkin, A.F., 2008c. Mesoscale to submesoscale transition in the california current system. part II: frontal processes. *J. Phys. Oceanogr.* 38 (1), 44–64. doi:10.1175/2007JPO3672.1.
- Capet, X., McWilliams, J.C., Molemaker, M.J., Shchepetkin, A.F., 2008d. Mesoscale to submesoscale transition in the california current system. part III: energy balance and flux. *J. Phys. Oceanogr.* 38 (1), 2256–2269. doi:10.1175/2008JPO3810.1.
- Charney, J.G., 1971. Geostrophic turbulence. *J. Atmos. Sci.* 28 (6), 1087–1095. doi:10.1175/1520-0469(1971)028<1087:GT>2.0.CO;2.
- Cole, S.T., Timmermans, M.-L., Toole, J.M., Krishfield, R.A., Thwaites, F.T., 2013. Ekman veering, internal waves, and turbulence observed under arctic sea ice. *J. Phys. Oceanogr.* 44 (5), 1306–1328. doi:10.1175/JPO-D-12-0191.1.
- D'Asaro, E.A., 1985. The energy flux from the wind to near-inertial motions in the surface mixed layer. *J. Phys. Oceanogr.* 15, 1043–1059.
- Dee, D., Uppala, S., Simmons, A., Berrisford, P., Poli, P., Kobayashi, S., Andrae, U., Balmaseda, M., Balsamo, G., Bauer, P., et al., 2011. The era-interim reanalysis: configuration and performance of the data assimilation system. *Q. J. R. Meteorol. Soc.* 137 (656), 553–597.
- Denbo, D.W., Skillingstad, E.D., 1996. An ocean large-eddy simulation model with application to deep convection in the greenland sea. *J. Geophys. Res.* 101 (C1), 1095–1110.
- Dosser, H.V., Rainville, L., Toole, J.M., 2014. Near-inertial internal wave field in the canada basin from ice-tethered profilers. *J. Phys. Oceanogr.* 44 (2), 413–426. doi:10.1175/JPO-D-13-0117.1.
- Fox-Kemper, B., Ferrari, R., Hallberg, R., 2008. Parameterization of mixed layer eddies. part I: theory and diagnosis. *J. Phys. Oceanogr.* 38 (6), 1145–1165. doi:10.1175/2007JPO3792.1.
- Gawarkiewicz, G., Chapman, D.C., 1995. A numerical study of dense water formation and transport on a shallow, sloping continental shelf. *J. Geophys. Res.* 100 (C3), 4489. doi:10.1029/94JC01742.
- Goosse, H., Deleersnijder, E., Fichefet, T., England, M.H., 1999. Sensitivity of a global coupled ocean-sea ice model to the parameterization of vertical mixing. *J. Geophys. Res.* 104 (C6), 13681–13695. doi:10.1029/1999JC900099.
- Gula, J., Molemaker, M.J., McWilliams, J.C., 2014. Submesoscale cold filaments in the gulf stream. *J. Phys. Oceanogr.* 44 (10), 2617–2643. doi:10.1175/JPO-D-14-0029.1.
- Hibler III, W.D., 1980. Modeling a variable thickness sea ice cover. *Mon. Weather Rev.* 108 (12), 1943–1973. doi:10.1175/1520-0493(1980)108<1943:MAVTSI>2.0.CO;2.
- Hoskins, B., 1982. The mathematical theory of frontogenesis. *Annu. Rev. Fluid Mech.* 14 (1), 131–151.
- Jackett, D.R., McDougall, T.J., 1995. Minimal adjustment of hydrographic profiles to achieve static stability. *J. Atmos. Oceanic Technol.* 12 (2), 381–389. doi:10.1175/1520-0426(1995)012<0381:MAOHTP>2.0.CO;2.
- Jackson, J.M., Carmack, E., McLaughlin, F., Allen, S.E., Ingram, R., 2010. Identification, characterization, and change of the near-surface temperature maximum in the canada basin, 1993–2008. *J. Geophys. Res.* 115 (C5).
- Jones, H., Marshall, J., 1993. Convection with rotation in a neutral ocean: a study of open-ocean deep convection. *J. Phys. Oceanogr.* 23, 1009–1039.
- Kaiser, J.F., Kuo, F.F., 1966. System analysis by digital computer. Wiley.
- Kara, A.B., 2003. Mixed layer depth variability over the global ocean. *J. Geophys. Res.* 108 (C3), 1–15. doi:10.1029/2000JC000736.
- Klein, P., Lapeyre, G., 2009. The oceanic vertical pump induced by mesoscale and submesoscale turbulence. *Ann. Rev. Mar. Sci.* 1 (1), 351–375. doi:10.1146/annurev.marine.010908.163704.
- Large, W., McWilliams, J., Doney, S., 1994. Oceanic vertical mixing: a review and a model with a nonlocal boundary layer parameterization. *Rev. Geophys.* 32 (4), 363–403.
- Legg, S., McWilliams, J., Gao, J., 1998. Localization of deep ocean convection by a mesoscale eddy. *J. Phys. Oceanogr.* 944–970.
- Leith, C., 1968. Diffusion approximation for two-dimensional turbulence. *Phys. Fluids* 11, 671–672. doi:10.1063/1.1691968.
- Leith, C., 1996. Stochastic models of chaotic systems. *Physica D* 98, 481–491.
- Levine, M.D., Paulson, C.A., Morison, J.H., 1985. Internal waves in the arctic ocean: comparison with lower-latitude observations. *J. Phys. Oceanogr.* 15 (6), 800–809. doi:10.1175/1520-0485(1985)015<0800:IWITAO>2.0.CO;2.
- Lévy, M., Klein, P., Treguier, A.-M., 2001. Impact of sub-mesoscale physics on production and subduction of phytoplankton in an oligotrophic regime. *J. Mar. Res.* 59 (4), 535–565. doi:10.1357/002224001762842181.
- Lumpkin, R., Elipot, S., 2010. Surface drifter pair spreading in the north atlantic. *J. Geophys. Res.* 115 (C12), 1–20. doi:10.1029/2010JC006338.
- Luo, H., Bracco, A., Cardona, Y., McWilliams, J.C., 2016. Submesoscale circulation in the northern gulf of mexico: surface processes and the impact of the freshwater river input. *Ocean Modell.* 101, 68–82. doi:10.1016/j.ocemod.2016.03.003.
- Magaldi, M.G., Haine, T.W.N., 2012. Hydrostatic and non-hydrostatic simulations of the east greenland spill jet. *Deep-Sea Res. Part I* 14, 13372. doi:10.1016/j.dsr.2014.10.008.
- Mahadevan, A., Tandon, A., 2006. An analysis of mechanisms for submesoscale vertical motion at ocean fronts. *Ocean Modell.* 14 (3–4), 241–256. doi:10.1016/j.ocemod.2006.05.006.
- Mahadevan, A., Thomas, L.N., Tandon, A., 2008. Comment on “Eddy/wind interactions stimulate extraordinary mid-ocean plankton blooms”. *Science* 320 (5875), 448b–448b. doi:10.1126/science.1152111.448b–448b.
- Marshall, J., Hill, C., Perelman, L., Adcroft, A., 1997. Hydrostatic, quasi-hydrostatic, and nonhydrostatic ocean modeling. *J. Geophys. Res.* 102 (C3), 5733–5752.
- Maykut, G., McPhee, M.G., 1995. Solar heating of the arctic mixed layer. *J. Geophys. Res.* 100 (C12), 24691–24703.
- Maykut, G.A., 1982. Large-scale heat exchange and ice production in the central arctic. *J. Geophys. Res.* 87 (C10), 7971–7984.
- McComas, C.H., Bretherton, F.P., 1977. Resonant interaction of oceanic internal waves. *J. Geophys. Res.* 82 (9), 1397–1412. doi:10.1029/JC082i009p01397.
- McGillicuddy, D.J., Anderson, L.A., Bates, N.R., Bibby, T., Buesseler, K.O., Carlson, C.A., Davis, C.S., Ewart, C., Falkowski, P.G., Goldthwait, S.A., Hansell, D.A., Jenkins, W.J., Johnson, R., Kosnyrev, V.K., Ledwell, J.R., Li, Q.P., Siegel, D.A., Steinberg, D.K., 2007. Eddy/wind interactions stimulate extraordinary mid-ocean plankton blooms. *Science* 316 (5827), 1021–1026. doi:10.1126/science.1136256.
- McPhee, M.G., 1992. Turbulent heat flux in the upper ocean under sea ice. *J. Geophys. Res.* 97 (C4), 5365–5379.
- McPhee, M.G., 2003. Ocean-to-ice heat flux at the north pole environmental observatory. *Geophys. Res. Lett.* 30 (24), 2274. doi:10.1029/2003GL018580.
- McWilliams, J.C., 2008. Fluid dynamics at the margin of rotational control. *Environ. Fluid Mech.* 8 (5–6), 441–449. doi:10.1007/s10652-008-9081-8.
- Mensa, J.A., Garraffo, Z.D., Griffa, A., Özgökmen, T.M., Haza, A.C., Veneziani, M., 2013. Seasonality of the submesoscale dynamics in the gulf stream region. *Ocean Dyn.* 63 (8), 923–941. doi:10.1007/s10236-013-0633-1.
- Mensa, J.A., Özgökmen, T.M., Poje, A.C., Imberger, J., 2015. Material transport in a convective surface mixed layer under weak wind forcing. *Ocean Modell.* 96, 226–242. doi:10.1016/j.ocemod.2015.10.006.
- Molemaker, M.J., McWilliams, J.C., Capet, X., 2010. Balanced and unbalanced routes to dissipation in an equilibrated eddy flow. *J. Fluid Mech.* 654, 35–63. doi:10.1017/S0022112009993272.
- Muller, P., Molemaker, M.J., McWilliams, J., 2005. Routes to Dissipation in the Ocean: The 2D/3D Turbulence Conundrum. In: *Marine Turbulence: Theories, Observations and Models*. Cambridge University Press, pp. 397–405.
- National Academies Report (NAS), 2014. Responding to oil spills in the u.s. arctic marine environment. The National Academies Press, Washington, DC doi:10.17226/18625.
- Perovich, D.K., Elder, B., 2002. Estimates of ocean heat flux at SHEBA. *Geophys. Res. Lett.* 29 (9).
- Phillips, N.A., 1963. Geostrophic motion. *Rev. Geophys.* 1 (2), 123. doi:10.1029/RG001i002p00123.

- Poje, A.C., Ozgökmen, T.M., Lipphardt, B.L., Haus, B.K., Ryan, E.H., Haza, A.C., Jacobs, G.A., Reniers, A.J.H.M., Olascoaga, M.J., Novelli, G., Griffa, A., Beron-Vera, F.J., Chen, S.S., Coelho, E., Hogan, P.J., Kirwan, A.D., Huntley, H.S., Mariano, A.J., 2014. Submesoscale dispersion in the vicinity of the deepwater horizon spill. *Proc. Natl. Acad. Sci. U.S.A.* 111 (35), 12693–12698. doi:10.1073/pnas.1402452111.
- Rainville, L., Woodgate, R.A., 2009. Observations of internal wave generation in the seasonally ice-free arctic. *Geophys. Res. Lett.* 36 (23), 1–5. doi:10.1029/2009GL041291.
- Rampal, P., Weiss, J., Dubois, C., Campin, J.M., 2011. IPCC Climate models do not capture arctic sea ice drift acceleration: consequences in terms of projected sea ice thinning and decline. *J. Geophys. Res.* 116 (9), 1–17. doi:10.1029/2011JC007110.
- Rhines, P.B., 1979. Geostrophic turbulence. *Annu. Rev. Fluid Mech.* 11. doi:10.1002/anie.200900101. 401–41
- Sasaki, H., Klein, P., Qiu, B., Sasai, Y., 2014. Impact of oceanic-scale interactions on the seasonal modulation of ocean dynamics by the atmosphere. *Nat. Commun.* 5, 5636. doi:10.1038/ncomms6636.
- Semtner, A.J., 1976. A model for the thermodynamic growth of sea ice in numerical investigations of climate. *J. Phys. Oceanogr.* 6 (3), 379–389. doi:10.1175/1520-0485(1976)006(0379:AMFTTG)2.0.CO;2.
- Semtner, A.J., 1984. On modelling the seasonal thermodynamic cycle of sea ice in studies of climatic change. *Clim. Change* 6 (1), 27–37. doi:10.1007/BF00141666.
- Serreze, B.M.C., 2007. Arctic climate change: where reality exceeds expectations. *Arctic* 5 (1), 1–4.
- Skyllingstad, E.D., 2001. Turbulence beneath the sea ice and leads. *J. Geophys. Res.* 106, 2477–2497.
- Smedsrud, L.H., Martin, T., 2015. Grease ice in basin-scale sea-ice ocean models. *Ann. Glaciol.* 56 (69), 295–306. doi:10.3189/2015AoG69A765.
- Stone, P., 1966. Frontogenesis by horizontal wind deformation fields. *J. Atmos. Sci.* 23, 455–465.
- Stroeve, J., Holland, M.M., Meier, W., Scambos, T., Serreze, M., 2007. Arctic sea ice decline: faster than forecast. *Geophys. Res. Lett.* 34 (9), 1–5. doi:10.1029/2007GL029703.
- Thomas, L., Tandon, A., Mahadevan, A., 2008. Submesoscale processes and dynamics. *Ocean Modell.* 177, 17–38.
- Thomas, L.N., Taylor, J.R., Ferrari, R., Joyce, T.M., 2013. Symmetric instability in the gulf stream. *Deep-Sea Res. Part II* 91, 96–110. doi:10.1016/j.dsr2.2013.02.025.
- Timmermann, R., Beckmann, A., 2004. Parameterization of vertical mixing in the weddell sea. *Ocean Modell.* 6 (1), 83–100. doi:10.1016/S1463-5003(02)00061-6.
- Timmermans, M.-L., 2015. The impact of stored solar heat on arctic sea ice growth. *Geophys. Res. Lett.* 42 (May), 1–8. doi:10.1002/2015GL064541.
- Timmermans, M.-L., Cole, S., Toole, J., 2012. Horizontal density structure and restratification of the Arctic ocean surface layer. *J. Phys. Oceanogr.* 42 (4), 659–668. doi:10.1175/JPO-D-11-0125.1.
- Timmermans, M.-L., Jayne, S.R., 2016. The arctic ocean spices up. *J. Phys. Oceanogr.* 46 (4), 1277–1284.
- Timmermans, M.-L., Proshutinsky, A., Golubeva, E., Jackson, J.M., Krishfield, R., McCall, M., Platov, G., Toole, J., Williams, W., Kikuchi, T., et al., 2014. Mechanisms of Pacific summer water variability in the Arctic's Central Canada Basin. *J. Geophys. Res.* 119 (11), 7523–7548.
- Timmermans, M.-L., Winsor, P., 2013. Scales of horizontal density structure in the Chukchi Sea surface layer. *Cont. Shelf Res.* 52, 39–45.
- Toole, J.M., Timmermans, M.-L., Perovich, D.K., Krishfield, R.A., Proshutinsky, A., Richter-Menge, J., 2010. Influences of the ocean surface mixed layer and thermohaline stratification on arctic sea ice in the central canada basin. *J. Geophys. Res.* 115 (C10).
- Veneziani, M., Griffa, A., Garraffo, Z., Mensa, J.A., 2014. Barrier layers in the tropical south atlantic: mean dynamics and submesoscale effects. *J. Phys. Oceanogr.* 44 (1), 265–288. doi:10.1175/JPO-D-13-064.1.
- Walsh, J.E., 1983. The role of sea ice in climatic variability: theories and evidence 1. *Atmos. Ocean* 21 (3), 229–242. doi:10.1080/07055900.1983.9649166.
- Wettlaufer, J., 1991. Heat flux at the ice-ocean interface. *J. Geophys. Res.* 96 (C4), 7215–7236.
- Zhang, J., Hibler, W.D., 1997. On an efficient numerical method for modeling sea ice dynamics. *J. Geophys. Res.* 102 (C4), 8691. doi:10.1029/96JC03744.